Journal of Marine Research, 56, 1–40, 1998

Journal of
MARINE RESEARCH

Volume 56, Number 1

Enhanced dispersion of near-inertial waves in an idealized geostrophic flow

by N. J. Balmforth[1], Stefan G. Llewellyn Smith[1] and W. R. Young[1]

ABSTRACT

This paper presents a simplified model of the process through which a geostrophic flow enhances the vertical propagation of near-inertial activity from the mixed layer into the deeper ocean. The geostrophic flow is idealized as steady and barotropic with a sinusoidal dependence on the north-south coordinate; the corresponding streamfunction takes the form $\psi = -\Psi \cos(2\alpha y)$. Near-inertial oscillations are considered in linear theory and disturbances are decomposed into horizontal and vertical normal modes. For this particular flow, the horizontal modes are given in terms of Mathieu functions. The initial-value problem can then be solved by projecting onto this set of normal modes. A detailed solution is presented for the case in which the mixed layer is set into motion as a slab. There is no initial horizontal structure in the model mixed layer; rather, horizontal structure, such as enhanced near-inertial energy in regions of negative vorticity, is impressed on the near-inertial fields by the pre-existing geostrophic flow.

Many details of the solution, such as the rate at which near-inertial activity in the mixed layer decays, are controlled by the nondimensional number, $\Upsilon = 4\Psi f_0/H_{\mathrm{mix}}^2 N_{\mathrm{mix}}^2$, where f_0 is the inertial frequency, H_{mix} is the mixed-layer depth, and N_{mix} is the buoyancy frequency immediately below the base of the mixed layer. When Υ is large, near-inertial activity in the mixed layer decays on a time-scale $H_{\mathrm{mix}} N_{\mathrm{mix}}/\alpha^2 \Psi^{3/2} f_0^{1/2}$. When Υ is small, near-inertial activity in the mixed layer decays on a time-scale proportional to $N_{\mathrm{mix}}^2 H_{\mathrm{mix}}^2/\alpha^2 \Psi^2 f_0$.

1. Introduction

The vertical propagation of near-inertial oscillations (NIOs) from the mixed layer into the thermocline is a crucial ingredient in current conceptions of how the upper ocean is mixed. Local violations of the Miles-Howard stability criterion (e.g. Polzin, 1996) are

---

[1] Scripps Institution of Oceanography, University of California at San Diego, La Jolla, California, 92093-0230, U.S.A.

thought to be created by the arrival of internal waves that are originally generated at either the top or the bottom of the ocean. As far as surface generation by wind events is concerned, one difficulty with this scenario is the very slow propagation rate of NIOs with length scales characteristic of the atmospheric forcing mechanism. Gill (1984) estimated that an NIO with a horizontal length scale of 1000 km will remain in the mixed layer for longer than one year. On the other hand, observations do show that after a storm the near-inertial energy in the mixed layer returns to background levels on a time scale of ten to twenty days (e.g., D'Asaro *et al.,* 1995; van Meurs, 1998). The implication is that at least part of this decay is associated with vertical transmission of near-inertial excitation into the upper ocean.

D'Asaro (1989) suggested a partial resolution of this problem; he showed that the β-effect results in a steady increase of the north-south wavenumber of the NIO with time: $l(t) = l(0) - \beta t$. Because the vertical group velocity of near-inertial waves is $c_g \approx -N^2(k^2 + l^2)/2f_0m^3$, the steady increase in l accelerates vertical propagation. However this 'β-dispersion' is only effective for the low vertical wavenumbers (notice that $c_g \propto m^{-3}$), which typically contain about 20% to 50% of the initial energy; see Zervakis and Levine (1995). But β-dispersion cannot explain the vertical propagation of the remaining energy, nor the transmission of the *near-inertial shear,* both of which are contained in the higher order modes.

The mechanism which is the focus of this paper is the refraction of NIOs by mesoscale eddies. Ray tracing studies have shown that geostrophic vorticity has an important refractive effect on near-inertial activity (Kunze, 1985). Consequently, several authors have suggested that the mesoscale eddy field plays a role in spatially modulating near-inertial activity (Weller *et al.,* 1991) and that enhanced vertical transmission is associated with this induced spatial structure. Indications of such an effect can be seen in numerical solutions, such as those of Klein and Treguier (1995), D'Asaro (1995a), van Meurs (1998) and Lee and Niiler (1998).

Additional evidence that the mesoscale eddy field accelerates the downward propagation of near-inertial oscillations comes from a recent theory by Young and Ben Jelloul (1997). This calculation involves an asymptotic reduction of the problem that filters the fast inertial oscillations and isolates the slower subinertial evolution of the amplitude. Young and Ben Jelloul employ the resulting reduced equations to show that the rectified effect of small- (relative to the initial scale of the NIO) scale geostrophic eddies can induce vertical dispersion of near-inertial waves. In this paper, we continue in the vein proposed by Young and Ben Jelloul. We use their reduced description to study vertical dispersion induced by mesoscale motions. One important advantage of this approach over ray-tracing is that it is not necessary to assume that the scale of the near-inertial waves is much less than that of the mesoscale eddies. Indeed, in the ocean, near-inertial waves are forced on the large spatial scales characteristic of atmospheric storm systems so that the WKB approximation is not applicable.

Our larger purpose in this work is to lay the wave-mechanical foundation for a theory of

NIO propagation through the strongly inhomogeneous environment of the mesoscale eddy field. But we must start with a simple theoretical formulation rather than with complicated models of geostrophic turbulence. In this paper, in fact, we attempt only to construct the simplest model we can think of which has some expectation of representing the real physical situation of very large-scale, near-inertial excitation superposed on a smaller scale geostrophic flow.

The simplified model is similar to the initial value problem of Gill (1984): at $t = 0$ the mixed layer moves as a slab and the deeper water is motionless. Gill considered background states without barotropic flow and modulated the initial slab velocity with a horizontal structure proportional to $\cos ly$. In Gill's problem, the lengthscale l^{-1} is vital in setting the rate at which the near-inertial activity in the mixed layer decays; if $l = 0$ then the mixed layer oscillates unendingly at precisely the inertial frequency; there is no vertical transmission, and no decay of the inertial oscillations in the mixed layer. We depart from Gill's analysis by introducing a background geostrophic flow. We show that, even if initial conditions are horizontally homogeneous ($l = 0$), the pre-existing geostrophic flow impresses horizontal structure on the near-inertial motion, and a relatively rapid vertical transmission ensues. We idealize this 'background' as a steady barotropic unidirectional velocity with sinusoidal variation: $\psi = -\Psi \cos 2\alpha y$.

We use a single sinusoid, $\psi \propto \cos(2\alpha y)$, as a background flow because the model is intended to represent the propagation of NIOs in a simple environment, such as the site of the Ocean Storms experiment in the Northeast Pacific (see D'Asaro *et al.,* 1995). We are not concerned with near-inertial propagation through spatially localized features such as intense jet (for example, Rubenstein and Roberts, 1986; Wang, 1991; Klein and Treguier, 1995) or Gulf Stream Rings (Kunze *et al.,* 1995; Lee and Niiler, 1998).

Our goal is to answer several basic questions within the context of the simple model outlined above. These questions are:

(i) How rapidly do the inertial oscillations in the mixed layer decay, and what features of the background determine the timescale of this decay?

(ii) Does the near-inertial activity in the mixed layer develop strong spatial modulations during the decay process?

(iii) Does the dispersal of near-inertial waves into the upper ocean result in the formation of isolated maxima in energy below the mixed layer?

The first question is directed at the issue of the decay of near-inertial energy and shear in the mixed layer: given that β-dispersion is ineffective for the high vertical modes, can the refractive effects of a geostrophic flow result in enhanced vertical propagation of small vertical scales? The second and third questions are motivated by observations made during the Ocean Storms experiment. First, using drifter data, van Meurs (1998) observed that, depending on spatial location, near-inertial oscillations in the mixed layer disappear on timescales which vary between 2 days and 20 days. Second, the mooring data summarized by D'Asaro *et al.* (1995) showed that as the inertial energy in the mixed layer decreases, a strong maximum in inertial energy appears at around 100 m (this was called a 'beam').

Our solution method is an expansion in the normal modes (both horizontal and vertical) of the problem; the details of these modes, and how we superpose them to solve the initial value problem, are given in Sections 2 through 4. Section 5 deals with visualizing the results. In Section 6 we discuss some limiting cases in which analytical approximations provide insight. We sum up in Section 7.

2. Formulation for a barotropic and unidirectional geostrophic flow

Our point of departure is the NIO equation of Young and Ben Jelloul. To leading order, the NIO velocity field, (u, v, w), buoyancy, b, and pressure, p, are expressed in terms of a complex field, $\mathscr{A}(x, y, z, t)$:

$$\begin{aligned} u + \mathrm{i}v &= e^{-\mathrm{i}f_0t} L\mathscr{A}, \\ w &= -\frac{1}{2} f_0^2 N^{-2}(\mathscr{A}_{zx} - \mathrm{i}\mathscr{A}_{yz})e^{-\mathrm{i}f_0t} + c.c., \\ b &= \frac{\mathrm{i}}{2} f_0(\mathscr{A}_{zx} - \mathrm{i}\mathscr{A}_{yz})e^{-\mathrm{i}f_0t} + c.c., \\ p &= \frac{\mathrm{i}}{2} f_0(\mathscr{A}_{x} - \mathrm{i}\mathscr{A}_{y})e^{-\mathrm{i}f_0t} + c.c., \end{aligned} \tag{2.1a–d}$$

where L is a differential operator defined by

$$L\mathscr{A} \equiv (f_0^2 N^{-1}\mathscr{A}_z)_z, \tag{2.2}$$

and $N(z)$ is the buoyancy frequency. Thus, the complex function $\mathscr{A}$ concisely describes all of the NIO fields.

If the background geostrophic flow is barotropic when $\mathscr{A}$ evolves according to the equation,

$$L\mathscr{A}_t + \frac{\partial(\psi, L\mathscr{A})}{\partial(x, y)} + \frac{\mathrm{i}}{2} f_0\nabla^2\mathscr{A} + \mathrm{i}\left(\beta y + \frac{1}{2}\zeta\right) L\mathscr{A} = 0. \tag{2.3}$$

In (2.3), $\psi(x, y)$ is the steady, barotropic streamfunction and $\zeta \equiv \nabla^2\psi$ is the corresponding vorticity. Throughout this paper ∇^2 is the horizontal Laplacian, i.e., $\nabla^2 = \partial_x^2 + \partial_y^2$. The boundary condition is that $\mathscr{A}_z = 0$ at the top and bottom of the ocean; from (2.1b) this ensures that w vanishes on the boundaries.

The approximate description in (2.3) is obtained by applying a multiple timescale approximation to the linearized primitive equations; the linearization is around the geostrophic background flow ψ. The small parameter in the expansion is essentially $(\omega - f_0)/f_0$; that is, the departure of the wave frequency from the inertial frequency. There is no assumption of spatial scale separation between the geostrophic background flow and the near-inertial wave. The evolution equation in (2.3) displays the processes which determine the subinertial evolution of the near-inertial part of the wave spectrum; namely, advection, dispersion and refraction by the combination $\beta y + (\zeta/2)$.

In Gill's (1984) notation, the Sturm-Liouville problem associated with the linear operator L is

$$L\hat{p}_n + f_0^2 c_n^{-2} \hat{p}_n = 0, \tag{2.4}$$

where the eigenvalue, $c_n = f_0 R_n$, is the speed of mode n and R_n is the Rossby radius. With the barotropic idealization, $\psi_z = 0$, one can project $\mathscr{A}$ onto the basis set in (2.4):

$$\mathscr{A}(x, y, z, t) = \sum_{n=1}^{\infty} \mathscr{A}_n(x, y, t)\hat{p}_n(z). \tag{2.5}$$

Each modal amplitude then satisfies the Schrödinger-like equation,

$$\frac{\partial \mathscr{A}_n}{\partial t} + \frac{\partial(\psi, \mathscr{A}_n)}{\partial(x, y)} + \mathrm{i}\left(\beta y + \frac{1}{2}\zeta\right)\mathscr{A}_n = \frac{\mathrm{i}\hbar_n}{2}\nabla^2 \mathscr{A}_n, \tag{2.6}$$

where

$$\hbar_n \equiv f_0 R_n^2, \tag{2.7}$$

is the 'dispersivity' of mode n. We will solve (2.6) as an initial value problem in Section 4.

To make an analogy with quantum mechanics, rewrite Eq. (2.6) as

$$\mathrm{i}\hbar_n \frac{\partial \mathscr{A}_n}{\partial t} = \frac{1}{2}(\mathrm{i}\hbar_n \nabla - \mathbf{u})^2 \mathscr{A}_n + V_n \mathscr{A}_n, \tag{2.8}$$

where

$$\begin{aligned} V_n &\equiv \hbar_n\left[\beta y + \frac{1}{2}\zeta\right] - \frac{1}{2}\mathbf{u}\cdot\mathbf{u}, \\ \mathbf{u} &= \mathbf{z} \times \nabla\psi. \end{aligned} \tag{2.9a,b}$$

After notational changes, Eq. (2.8) is the same as Schrödinger's equation for the motion of a particle (with mass $m = 1$) in a magnetic field $\nabla^2\psi\hat{\mathbf{z}}$. In this analogy, the geostrophic velocity, $\mathbf{u} = \mathbf{z} \times \nabla\psi$, is the vector potential of the magnetic field (usually denoted by $\mathbf{A}$ in quantum mechanics), and V_n is the potential function. The quantum analogy is flawed because the potential V_n contains the term $\mathbf{u}\cdot\mathbf{u}/2$ and there is no equivalent term in the quantum mechanical case. Nonetheless, the quantum analogy is suggestive and useful.[2]

---

[2] For instance, if $\psi = 0$, then (2.8) is equivalent to the motion of a particle falling in a uniform gravitational potential, $\hbar_n \beta y$. Thus, particles (i.e., near-inertial wave packets) accelerate toward the equator, with $g_n = \beta\hbar_n$. D'Asaro's (1989) result that $l(t) = l(0) - \beta t$ is the linear-in-time momentum increase occurring as a particle falls in a uniform gravitational field. The paths of wave packet centers in the (x, y)-plane are the parabolic trajectories of ballistically launched particles.

We now limit attention to zonal parallel flows; that is, $\psi_x = 0$ and $\zeta = \psi_{yy}$. One can then solve (2.6) by looking for normal mode solutions with

$$\mathscr{A}_n(x, y, t) = A_n(y) \exp(\mathrm{i}kx - \mathrm{i}\omega_n t). \tag{2.10}$$

The resulting eigenproblem for ω_n is

$$\hbar_n \frac{\mathrm{d}^2 A_n}{\mathrm{d}y^2} + [2\omega_n - \hbar_n k^2 - \Phi] A_n = 0, \tag{2.11}$$

where

$$\Phi(y) = \psi_{yy} - 2k\psi_y + 2\beta y. \tag{2.12}$$

In the remainder of this paper, we construct the solutions of the eigenproblem in (2.11), then solve the initial value problem.

Earlier studies of NIO interaction with geostrophic flows have emphasized that waves are concentrated in regions of negative $\zeta = \psi_{yy}$ (Kunze, 1985; Rubenstein and Roberts, 1986; Klein and Treguier, 1995). On the other hand, the quantum analogy suggests that the solution of (2.11) will be large in regions where Φ is negative (i.e., inside potential wells). Provided that $\Phi \approx \psi_{yy}$, there is agreement between these two approaches.

3. The normal modes for a sinusoidal shear flow

We now consider the sinusoidal barotropic flow with associated streamfunction

$$\psi = -\Psi \cos(2\alpha y), \tag{3.1}$$

where, for definiteness, we take $\Psi > 0$. We also take $\beta = 0$. The potential function, $\Phi(y)$ in (2.12), can then be put in the form

$$\Phi = 4\alpha\sqrt{\alpha^2 + k^2}\,\Psi \cos 2\eta, \qquad \eta \equiv \alpha y + \frac{\gamma}{2}, \tag{3.2a,b}$$

where

$$\sin\gamma = k/\sqrt{\alpha^2 + k^2}, \qquad \cos\gamma = \alpha/\sqrt{\alpha^2 + k^2}. \tag{3.2c,d}$$

Hence (2.11) can be written as

$$\frac{\mathrm{d}^2 A_n}{\mathrm{d}\eta^2} + (a - 2q\cos 2\eta) A_n = 0, \tag{3.3a}$$

where

$$a \equiv (2\omega - \hbar_n k^2)/\hbar_n \alpha^2, \qquad q \equiv 2\Psi\sqrt{1 + \alpha^{-2}k^2}/\hbar_n. \tag{3.3b,c}$$

The differential equation (3.3a) is Mathieu's equation (Abramowitz and Stegun, 1972).

From this point forward we take $k = 0$. It is clear from (3.2) and (3.3) that nonzero k has no qualitative effects provided that $k/\alpha \ll 1$; for NIOs forced by large-scale winds this is the case. In the special case $k = 0$ the Mathieu equation can also be derived directly from the primitive equations—see Appendix A.

a. Solutions of Mathieu's equation

Mathieu functions are examples of classical special functions and descriptions of them may be found in texts (e.g., Abramowitz and Stegun, 1972; Brillouin, 1946; McLachlan, 1947). However, these particular special functions are neither common, nor are they members of the hypergeometric family, and so we give a rudimentary discussion of them.

It follows from Floquet theory that every solution of Mathieu's equation (3.2) can be expressed in the form,

$$A_n(\eta) = e^{i\nu\eta}P(\eta; a, q), \tag{3.4}$$

where $\nu(a, q)$ (the "characteristic exponent," or Bloch wavenumber in quantum mechanics) is a (possibly complex) function of a and q, and $P(\eta; a, q)$ is a periodic function of period π. There is a special class of solutions in which $\nu(a, q) = 0$, so that A in (3.4) is a periodic function of η. These periodic functions are the 'Mathieu functions of integer order'; because $\nu = 0$, these functions exist only on a set of curves in the (a, q) parameter plane. These curves, displayed in Figure 20.1 of Abramowitz and Stegun (1972), define the eigenvalue, a, as a function of the parameter q.

The Mathieu functions of integer order, r, divide into even solutions, $ce_r(\eta, q)$, and into odd ones, $se_r(\eta, q)$; the integer index, $r = 0, 1, \ldots,$ is the horizontal mode number. These solutions have the eigenvalues, $a_r(q)$ and $b_r(q)$, respectively. Linear combinations of Mathieu functions of integer order can be used to represent any function which has the periodicity, $F(\eta) = F(\eta + \pi)$: this completeness is the basis of our solution in Section 4. More precisely, we will be concerned with solving the NIO equation subject to an initial condition which is uniform in the horizontal. That is, we are interested in a situation in which we need to express a constant initial condition in terms of the normal mode solutions. Since a constant is a (trivial) example of a function with period π, the particular solutions of (3.2) which we need are precisely the Mathieu functions of integer order. Moreover, since only even modes project onto that constant, we need only the Mathieu functions of even integer order, denoted by $ce_r(\eta, q)$. Hence, from this point forward, we focus entirely on these specific solutions; these modes are the building blocks used in Section 4. (We would need a more general class of modal solutions, including both the odd Mathieu functions, $se_r(\eta, q)$, and the other, nonperiodic solutions with $\nu \neq 0$, were we to consider an initial condition with more complicated horizontal structure.)

b. The Mathieu functions of even integer order

We use the package written by Shirts (1993), and available from http://gams.nist.gov, to compute the Mathieu functions of integer order. In Figures 1 and 2, we display the structure of the lower order, even Mathieu functions. In Figure 1a, we show the functions $ce_0(\eta, q)$ for various values of q. Notice that $ce_0(\eta, 0) = 1/\sqrt{2}$, but as q increases, the eigenmode $ce_0(\eta, q)$ becomes increasingly concentrated to the vicinity of $\eta = \pi/2$. This corresponds to a localization of the mode to the region where the geostrophic vorticity, $4\alpha^2\Psi \cos(2\eta)$, is negative (the minima of the quantum mechanical potential).

Figure 1b shows the same transition for the eigenfunction $ce_4(\eta, q)$. The localization is illustrated further in Figure 2, which shows $ce_r(\eta, 100)$ with $r = 0$, 1 and 2; the main point to note here is the general trend that the higher-order eigenmodes are less concentrated than the low-order modes.

The most physically relevant quantity is the eigenfrequency, $\omega_{r,n}$. In order to determine these modal frequencies, we need to first specify q, then obtain the appropriate eigenvalue, $a_r(q)$, from (3.2). Finally, using (3.3b),

$$\omega_{r,n} = \frac{1}{2}\alpha^2\hbar_n a_r(2\Psi/\hbar_n). \tag{3.5}$$

A more revealing way of representing the dispersion relation (3.5) is to observe from $L\mathscr{A}_n + R_n^{-2}\mathscr{A}_n = 0$ that the Rossby radius of deformation of the nth vertical mode, R_n, and the local vertical wavenumber, $m(z)$, are related by

$$m(z) = N(z)/f_0R_n. \tag{3.6}$$

On combining the above with (2.7) and (3.3c), we obtain

$$q = \frac{2\Psi f_0}{N^2}m^2. \tag{3.7}$$

The expression in (3.7) motivates the definition of a dimensionless vertical wavenumber as

$$\hat{m} \equiv \sqrt{\frac{2\Psi f_0}{N^2}}\,m, \tag{3.8a}$$

or, equivalently, $\hat{m} = \sqrt{q}$. Now define a dimensionless frequency as

$$\hat{\omega} \equiv 2\omega/|\zeta_{\min}|, \tag{3.8b}$$

where $\zeta_{\min} \equiv -4\alpha^2\Psi < 0$ is the most negative value of the geostrophic vorticity. These definitions put (3.5) into the compact form,

$$\hat{\omega} = \frac{1}{2\hat{m}^2}a_r(\hat{m}^2), \tag{3.9}$$

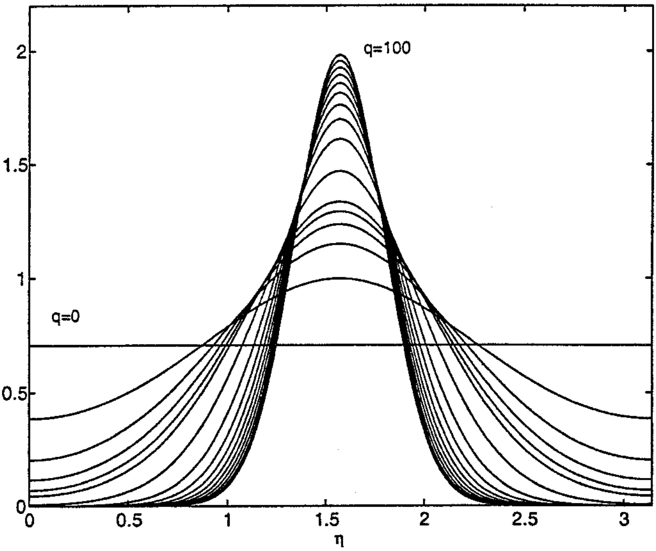
(a) Mathieu functions of order r=0

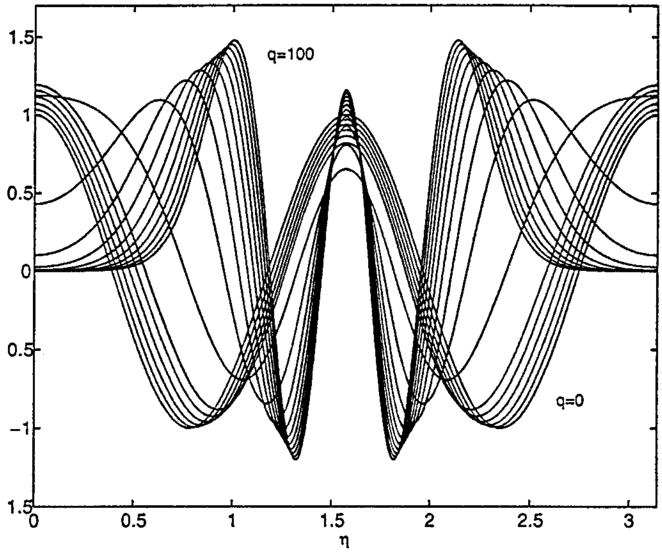
(b) Mathieu functions of order r=4

Figure 1. (a) Mathieu functions $ce_0(\eta, q)$ with $q = 0$ through 5, then $q = 10$, followed by steps of 10 until $q = 100$. (b) Mathieu functions $ce_4(\eta, q)$ at the same values of q as part (a). Notice that $ce_0(\eta, 0) = 1/\sqrt{2}$ and $ce_4(\eta, 0) = \cos(4\eta)$. As q increases both of these eigenfunctions become concentrated around the vorticity minimum at $\eta = \pi/2$.

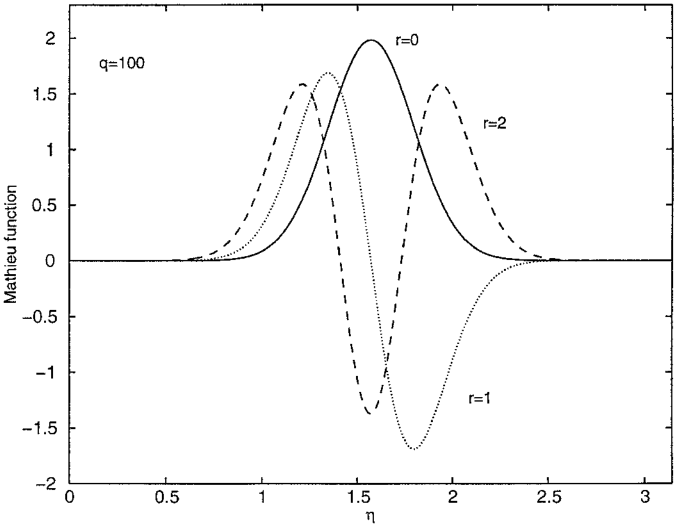

Figure 2. The three Mathieu functions $ce_0(\eta, 100)$, $ce_1(\eta, 100)$ and $ce_2(\eta, 100)$. As the index, r, increases the function becomes less localized. Notice also that ce_1 is antisymmetric around $\eta = \pi/2$. This antisymmetry ensures that ce_1 does not project onto 1 in the sum (3.11a).

where the index $r = 0, 1, \cdots$ is the horizontal mode number. In Figure 3 we show the dispersion relation of the even modes with $r = 0, 2, \cdots, 20$. All of the eigenbranches slowly asymptote to $\hat{\omega} = -1$, corresponding to a dimensional frequency shift of $\zeta_{\min}/2$ (cf., Kunze, 1985).

We summarize our progress by saying that there is a set of two-dimensional eigenfunctions, $\hat{p}_n(z)ce_r(\alpha y, 2\Psi/f_0R_n^2)$. The eigenfunctions are indexed by (n, r) and the eigenfrequencies are given by (3.5).

c. Representation of one as a sum of Mathieu eigenfunctions

In the next section we solve (2.6) as an initial value problem with $\mathcal{A}_n(y, t = 0) = 1$. This is accomplished by projecting the initial condition onto the eigenmodes described above; that is, by representing 1 as a sum of Mathieu functions. The orthogonality property,

$$\int_0^{2\pi} ce_\nu(\eta, q)ce_\mu(\eta, q)\, d\eta = \pi\delta_{\mu\nu}, \tag{3.10}$$

can be used to deduce the representation,

$$1 = \frac{1}{\pi}\sum_{r'=0}^{\infty} \Xi_{2r'}(q)ce_{2r'}(\eta, q), \tag{3.11a}$$

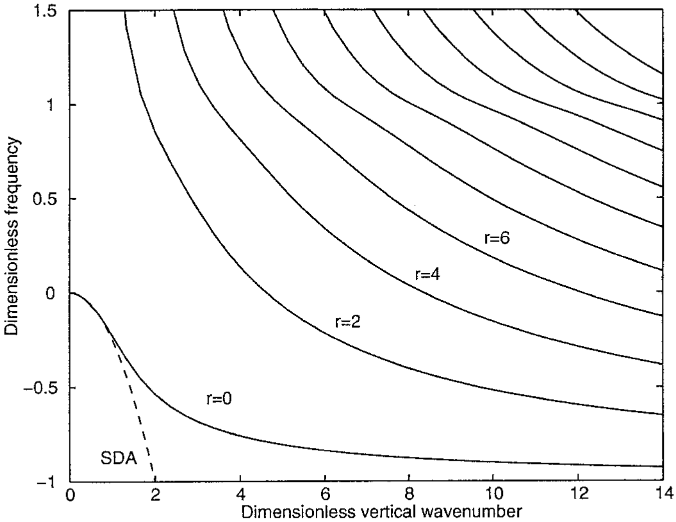

Figure 3. The dimensionless frequency, $\hat{\omega}$ in (3.8b), as a function of the dimensionless wavenumber $\hat{m} = \sqrt{q}$. We show only the dispersion relations of the eigenfunctions $ce_{2r'}(\eta, q)$ which appear in (3.11a) ($r' = 0$ through $r' = 10$). All of the curves asymptote to $\hat{\omega} = -1$. In anticipation of results from Section 6 we show the strong dispersion approximation as the dashed curve $\hat{\omega} = -\hat{m}^2/4$ labelled 'SDA'. Notice that the strong dispersion approximation captures only the $r = 0$ branch.

where

$$\Xi_r(q) \equiv \int_0^{2\pi} ce_r(\eta, q)\, d\eta. \tag{3.11b}$$

In the notation of Abramowitz and Stegun (1972), $\Xi_r(q) = A_0^r(q)$; due to our alternative use of 'A' we prefer to introduce the quantity in (3.11b). Because of symmetry, the odd eigenfunctions, $se_r(\eta, q)$, do not appear in the series (3.11a). There is also a further symmetry, evident in the graph of ce_1 in Figure 2, that removes the functions $ce_{2r'+1}(\eta, q)$ from the series (i.e., $\Xi_{2r'+1}(q) = 0$).

The series in (3.11a) converges very quickly; in fact, if $q = 0$ one term is exact. If $q \gg 1$ the convergence is still very fast. Figure 4 shows the partial sums of (3.11a) with $q = 100$. Using eleven terms (this is the truncation we employ in Section 5) the error is less than one percent.

4. The initial value problem

In this section we solve the initial value problem by projection onto the modes described above. Up to this point we have avoided making a particular choice of buoyancy profile $N(z)$. But now we need to specify the vertical modes and so we adopt Gill's (1984) model buoyancy profile which combines analytical simplicity with physical realism. Zervakis and

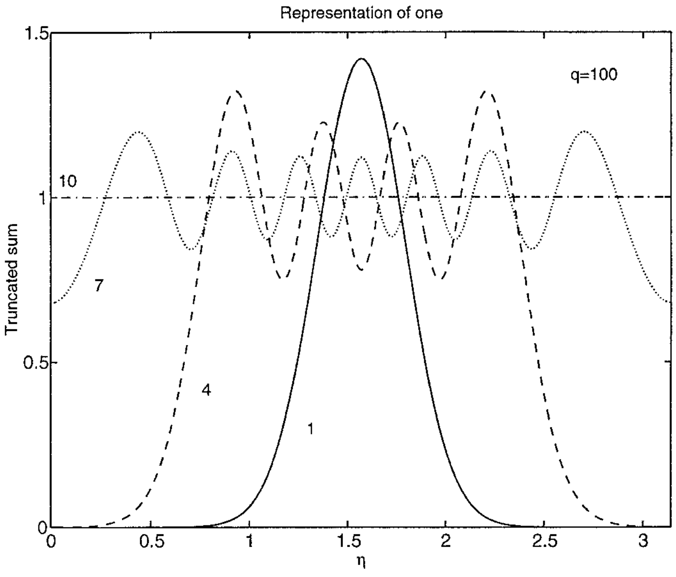

Figure 4. The series in (3.11a) truncated after the indicated number of terms. Because (3.11a) is representing a smooth, periodic function (viz., one) as a superposition of smooth periodic functions (viz., $ce_r(\eta, 100)$) there is no Gibbs' phenomenon and the error of the truncated sum eventually decays exponentially as the number of retained terms increases.

Levine (1995) provide some useful additional information concerning the properties of these vertical modes.

a. *Gill's buoyancy profile*

Gill's buoyancy profile is

$$N(z) = \begin{cases} 0, & \text{if } -H_{\text{mix}} < z < 0; \\ s/(z_0 - H - z), & \text{if } -H < z < -H_{\text{mix}}. \end{cases} \tag{4.1}$$

(Gill placed $z = 0$ at the bottom of the ocean; we prefer to use the convention that $z = 0$ is the surface of the ocean.) Typical values for the parameters are given in Table 1. As mentioned in Section 2, there is a set of Sturm-Liouville eigenfunctions that satisfy

$$\frac{d\hat{p}_n}{dz} = -N^2\hat{h}_n, \qquad c_n^2\frac{d\hat{h}_n}{dz} = \hat{p}_n, \tag{4.2a,b}$$

where $c_n = f_0R_n$ is the eigenspeed. Gill's analytic solution for $\hat{h}_n$ and $\hat{p}_n$ arises on solving (4.2a,b) with (4.1).

Figure 5 summarizes the solution of the eigenproblem by showing $q/n^2 = 2\Psi/f_0n^2R_n^2$ as a function of n. Figure 5 can be used to quickly estimate the value of q which is used in the solution of the horizontal eigenproblem (3.3a). For instance, suppose that one is interested

Table 1. Numerical values of the parameters used in the calculations. The numerical values of Ψ, α, Υ and T refer to the 'standard case' of Section 5b.

Quantity	Symbol	Typical numerical value
Ocean depth	H	4200 m
Mixed layer depth	H_{mix}	50 m
Stratification parameter	s	2.5 m s^{-1}
Vertical scale of N	z_0	4329.6 m
N at base of mixed layer	N_{mix}	0.01392 s^{-1}
Inertial frequency	f_0	$10^{-4}\ \mathrm{s}^{-1}$
Length scale of geostrophic flow	α^{-1}	80,000 m
Maximum geostrophic streamfunction	Ψ	4000 $\mathrm{m}^2\ \mathrm{s}^{-1}$
Minimum geostrophic vorticity	$\zeta_{\mathrm{min}} = -4\alpha^2\Psi$	$-2.5 \times 10^{-6}\ \mathrm{s}^{-1}$
Kinetic energy density	$K = (\alpha\Psi)^2$	$\frac{1}{400}\ \mathrm{m}^2\ \mathrm{s}^{-2}$
Time scale	$T = 2/\lvert\zeta_{\mathrm{min}}\rvert$	9.26 days
Nondimensional ocean depth	$\hat{H}$	83
Nondimensional stratification parameter	μ	0.139
Nondimensional geostrophic flow strength	Υ	3.302
Normalization constant	$\mathcal{N}$	1.200

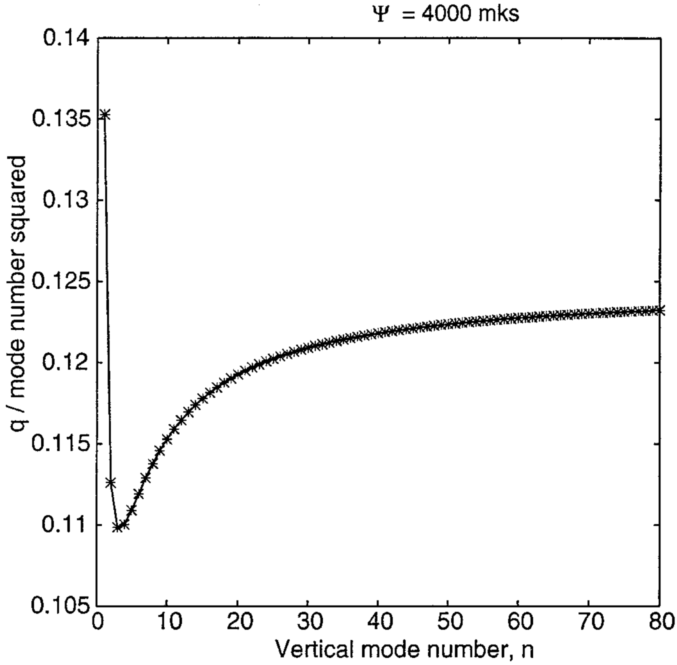

Figure 5. A plot of $2\Psi/n^2R_n^2f_0$ versus vertical mode number n. The modal speed $c_n = f_0R_n$ is the eigenvalue obtained from solving the vertical eigenproblem in (4.1) and (4.2). We use the numerical values from Table 1; i.e., $\Psi = 4000\ \mathrm{m}^2\ \mathrm{s}^{-1}$. Using the combination q/n^2 on the vertical axis removes the strongest dependence on the vertical mode number.

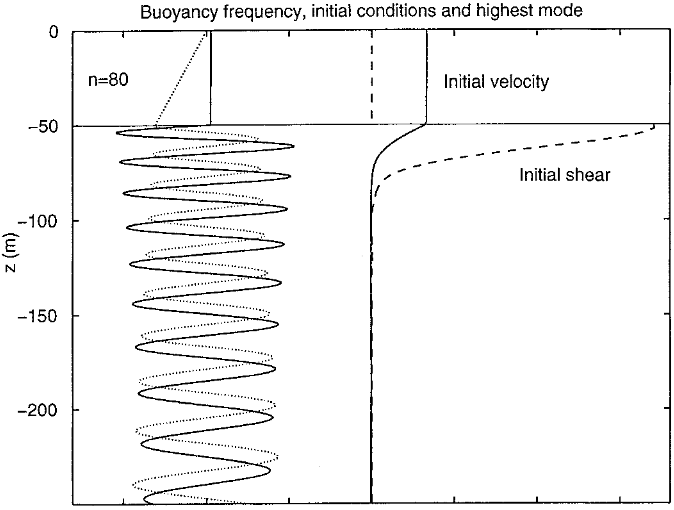

Figure 6. The initial velocity, $u_I(z)$, and the initial shear $du_I(z)/dz$ (solid and dashed respectively) calculated from (4.4). The highest vertical eigenmode, $n = 80$, is shown in the left-hand portion of the figure. The function $\hat{p}_{80}(z)$ is shown by the solid curve and $\hat{h}_{80}(z)$ by the dotted curve.

in vertical mode number $n = 10$ and $\Psi = 4000$ m^2 s^{-1}. Then it follows from Figure 5 that $q/(10)^2 = 0.115$, or $q = 11.5$. Using Figures 1 and 2, one can then get some impression of the structure of the horizontal modes with the common vertical mode number $n = 10$.

The eigenmodes in (4.2a) are orthogonal:

$$\int_0^H \hat{p}_n(z)\hat{p}_m(z)\,dz = (H_{\text{mix}}/\sigma_n)\delta_{mn}, \qquad \int_0^H N^2(z)\hat{h}_n(z)\hat{h}_m(z)\,dz = (H_{\text{mix}}/c_n^2\sigma_n)\delta_{mn}, \qquad (4.3\text{a,b})$$

where the normalization constant σ_n is defined in Eq. (A9) of Gill.[3]

b. The vertical structure of the initial condition

Gill considered an initial condition in which the mixed layer moves as a slab. Here, we use a modified form of Gill's initial condition. Specifically, we take

$$u_I(z) \equiv \sum_{n=1}^{80} \epsilon_n \sigma_n \hat{p}_n(z), \qquad \epsilon_n \equiv \mathcal{N} \exp(-n^2/600), \qquad (4.4\text{a,b})$$

and $v_I(z) = 0$. The normalization factor, $\mathcal{N}$ in (4.3b), is computed to ensure that $u_I(0) = 1$. The initial condition (4.3) is shown in Figure 6. As a result of truncating the sum at $n = 80$ and including the low pass filter, ϵ_n, there is now some initial excitation in about the first 20

---

[3] There is a misprint in (A9) of Gill. With the notation of that Appendix, the expression for σ_n should be:

$$\sigma_n = 2\epsilon\left(1 + \frac{\epsilon}{2}m^2\right)\left(m^2 + \frac{1}{4}[\epsilon + \xi_T(1 + \epsilon^2 m^2)]\right)^{-1}.$$

meters below the mixed layer. This is probably more realistic than a completely discontinuous initial condition. Further, since we are interested in examining the evolution of the vertical shear we must have an initial condition in which the shear is finite; the initial shear profile in Figure 6 is consistent with the observation of shear concentration at the base of the mixed layer.

Additional motivation for the initial condition in Figure 6 is provided by the very slow convergence of the unfiltered series to Gill's discontinuous initial velocity. For instance, if the unfiltered series is truncated after P terms, then the error is $O(1/P)$. Further, the initial condition defined by a truncated sum exhibits Gibbs' phenomenon; even with $P = 120$ terms there is unrealistic oscillatory structure at relatively deep levels. The filtering factor ϵ_n eliminates this “ringing’ and provides a strongly localized initial excitation.

c. Projection of the initial condition on the modes

We now represent $\mathscr{A}(y, z, t)$ as a sum of vertical normal modes, as in (2.5), and project the initial condition, $L\mathscr{A}(y, z, 0) = u_I(z)$ in (4.4), onto this basis set. The result is that

$$\mathscr{A}_n(y, 0) = -R_n^2\epsilon_n\sigma_n. \qquad (4.5)$$

Thus, after the projection on vertical normal modes, the problem is to solve

$$\frac{\partial \mathscr{A}_n}{\partial t} + 2i\alpha^2\Psi\cos(2\alpha y)\,\mathscr{A}_n = \frac{i}{2}\hbar_n\frac{\partial^2 \mathscr{A}_n}{\partial y^2}, \qquad (4.6)$$

with the initial condition in (4.5).

Next, we use (3.11a) to project the initial condition (4.5) onto horizontal eigenmodes. This gives:

$$\mathscr{A}_n(y, t) = -R_n^2\epsilon_n\sigma_n\sum_{r'=0}^{\infty}\Xi_{2r',n}\exp(-i\omega_{2r',n}t)\,ce_{2r'}(\alpha y, 2\Psi/\hbar_n), \qquad (4.7)$$

where $\Xi_{2r',n} \equiv \Xi_{2r'}(2\Psi/\hbar_n)$. The frequency of the mode with index $(2r', n)$ is, as before, $\omega_{2r',n} = \hbar_n\alpha^2 a_{2r'}(2\Psi/\hbar_n)/2$.

d. Reconstruction of the velocity and the shear

To reconstruct the final fields one must sum (4.7) over the vertical mode number, n. Thus, using (2.1a) with $L\hat{p}_n = -R_n^{-2}\hat{p}_n$, one finds that the horizontal velocities are given by

$$u + iv = e^{-if_0t}\sum_{n=1}^{80}\sum_{r'=0}^{10}\epsilon_n\sigma_n\Xi_{2r',n}\exp(-i\omega_{2r',n}t)\,ce_{2r'}(\alpha y, 2\Psi/\hbar_n)\,\hat{p}_n(z). \qquad (4.8)$$

The sum over r' in (4.8) has been truncated after eleven terms; this is more than enough to ensure convergence (see Fig. 4). In addition, one obtains from (4.8) the following expression for the vertical shear:

$$u_z + \mathrm{i}v_z = -e^{-\mathrm{i}f_0t}N^2 \sum_{n=1}^{80}\sum_{r'=0}^{10} \epsilon_n\sigma_n\Xi_{2r',n}\exp(-\mathrm{i}\omega_{2r',n}t)\, ce_{2r'}(\alpha y, 2\Psi/\hbar_n)\,\hat{h}_n(z), \qquad (4.9)$$

where $\hat{h}_n$ is defined in (4.2). The series in (4.8) and (4.9) are our solution of the initial value problem posed in Figure 6.

Before attempting visualization of the solution, let us examine the spectral decay of (4.8) and (4.9). Using the orthogonality relations in (4.3), the total squared velocity is

$$\int_0^{2\pi/\alpha}\int_0^H (u^2 + v^2)\,\mathrm{d}z\,\mathrm{d}y = \pi H_{\mathrm{mix}}\alpha^{-1}\sum_{n=1}^{80}\sum_{r'=0}^{10}\epsilon_n^2\sigma_n\Xi_{2r',n}^2, \qquad (4.10)$$

from which we can read off the fraction of energy contained in the mode (r', n):

$$\mathscr{E}_{2r',n} \equiv \epsilon_n^2\sigma_n\Xi_{2r',n}^2 \Bigg/ \sum_{n=1}^{80}\sum_{r'=0}^{10}\epsilon_n^2\sigma_n\Xi_{2r',n}^2. \qquad (4.11)$$

This modal energy fraction is shown in Figure 7a.

The modal content of the total squared shear is a little more difficult to estimate because the functions $N^2\hbar_n(z)$ are not orthogonal. Hence the total square shear,

$$\int_0^{2\pi/\alpha}\int_0^H (u_z^2 + v_z^2)\,\mathrm{d}z\,\mathrm{d}y, \qquad (4.12)$$

does not separate into a convenient sum over squares of modal amplitudes. However, the orthogonality relation (4.3b) shows that the functions $N\hat{h}_n(z)$ are orthogonal. Hence, we estimate the modal content of the mean square shear using the weighted average,

$$\int_0^{2\pi/\alpha}\int_0^H N^{-2}(u_z^2 + v_z^2)\,\mathrm{d}z\,\mathrm{d}y. \qquad (4.13)$$

Thence, the fraction of the weighted mean square shear in the mode (r', n) is given by

$$\mathscr{S}_{2r',n} \equiv \epsilon_n^2\sigma_n\Xi_{2r',n}^2 c_n^{-2} \Bigg/ \sum_{n=1}^{80}\sum_{r'=0}^{10}\varepsilon_n^2\sigma_n\Xi_{2r',n}^2 c_n^{-2}, \qquad (4.14)$$

which is shown in Figure 7b. Notice that the expression in (4.13) is proportional to an 'inverse Richardson number' averaged over the volume of the fluid. Thus $\mathscr{S}_{2r',n}$ in (4.14) is the contribution of mode $(2r', n)$ to the inverse Richardson number.

Figure 7 shows that the truncation in (4.8) is sufficient to resolve both the velocity and shear. The velocity is heavily concentrated in the low modes. In particular, the modes with horizontal mode number $r = 0$ contain over 85% of the energy. On the other hand, the shear is distributed more evenly over higher modes (note the different scales of the vertical axes in the two parts of Fig. 7).

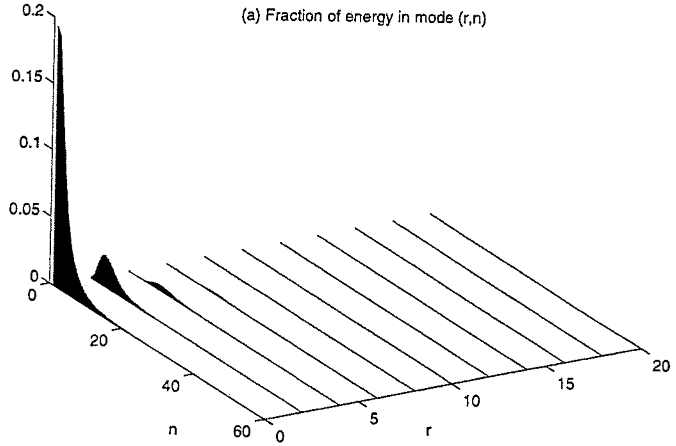

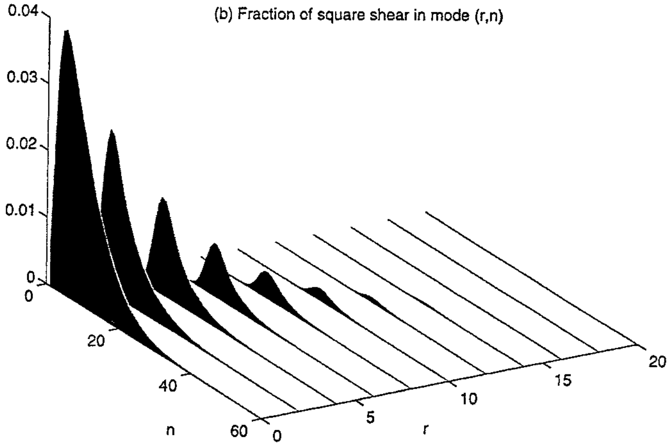

Figure 7. (a) Upper panel; the fraction of energy, $\mathscr{E}_{2r',n}$ in (4.11) in the mode $(2r', n)$. Notice that the axis is $r = 2r'$. Most of the energy is contained in the first two horizontal modes with $r' = 0$ and $r' = 1$. (b) Lower panel; the fraction of square shear (or inverse Richardson number), $\mathscr{S}_{2r',n}$ in (4.14), in mode $(2r', n)$. Note the different scales on the vertical axes in (a) and (b). As expected, higher modes make a more important contribution to the shear.

Another view of the initial excitation is shown in Figure 8 where $\mathscr{E}_{2r',n}$ is plotted against the dimensionless modal eigenfrequency, $\hat{\omega}$ in (3.9). It is significant that the eigenfrequencies with $\hat{\omega} \approx -1$ (that is, dimensional frequencies close to $\zeta_{\min}/2$) do not contain much energy. This might bear on D'Asaro's (1995b) unsuccessful attempt to observe a $\zeta/2$ frequency shift using the Ocean Storms data set. Our model initial condition simply does not excite modes with eigenfrequencies close to $\zeta_{\min}/2$. In fact, the concept of a spatially local frequency shift is usually meaningless when one has eigenmodes. The concept acquires some meaning if the eigenmodes are spatially localized near a potential minimum;

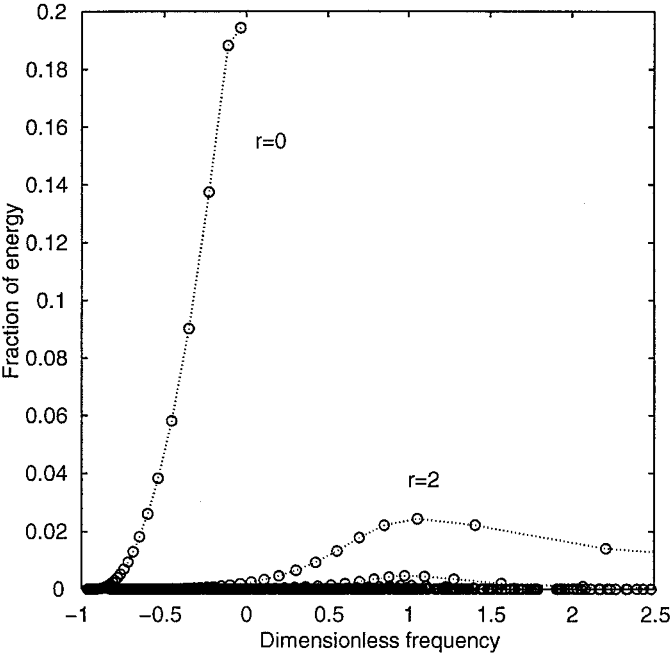

Figure 8. The fraction of energy in mode $(2r', n)$, $\mathscr{E}_{2r',n}$ in (4.11), plotted against the nondimensional modal frequency, $2\omega_{2r',n}/\zeta_{\min}$. The horizontal axis is truncated at $\hat{\omega} = 2.5$; there are higher frequencies in the series (4.8).

this is why the eigencurves in Figure 3 asymptote to $\hat{\omega} = -1$ (corresponding to $\zeta_{\min}/2$). But, to strongly excite such localized modes, we would need a very different initial condition.

5. Results

a. Dimensional considerations

To systematically discuss the results of parametric variations we must first consider the nondimensional form of the problem. As nondimensional independent variables we use

$$\hat{t} \equiv t/T, \qquad \eta \equiv \alpha y, \qquad \hat{z} = (z + H_{\text{mix}})/H_{\text{mix}}, \tag{5.1}$$

where, following our earlier definition of the nondimensional frequency in (3.8b), the timescale is $T = 2/|\zeta_{\min}|$. For the sinusoidal flow in (3.1) this choice of T is equivalent to

$$T \equiv \frac{1}{2\alpha^2\Psi}. \tag{5.2}$$

The nondimensional vertical coordinate is $-\hat{H} < \hat{z} < 1$, where the nondimensional ocean depth is $\hat{H} \equiv (H - H_{\text{mix}})/H_{\text{mix}}$. Notice that $\hat{z} = 0$ is the base of the mixed layer and $\hat{z} = 1$ is the ocean surface. The buoyancy frequency can be measured in units of its value directly beneath the mixed layer, N_{mix}; for the particular profile of (4.1), we then find

$$\hat{N}(\hat{z}) = \begin{cases} 0, & \text{if } 0 < \hat{z} < 1; \\ 1/(1 - 2\mu\hat{z}), & \text{if } -\hat{H} < z < 0. \end{cases} \tag{5.3}$$

where $\mu \equiv H_{\text{mix}}/2(z_0 + H_{\text{mix}} - H)$ and $N_{\text{mix}} \equiv s/(z_0 - H + H_{\text{mix}})$.

The nondimensional form of the $\mathscr{A}$ equation can then be written

$$\Upsilon[\hat{L}\mathscr{A}_{\hat{t}} + \mathrm{i}\cos 2\eta\, \hat{L}\mathscr{A}] + \mathrm{i}\mathscr{A}_{\eta\eta} = 0, \tag{5.4}$$

where $\hat{L}$ is the nondimensional differential operator,

$$\hat{L} = \partial_{\hat{z}}\hat{N}^{-2}\partial_{\hat{z}}. \tag{5.5}$$

The most important nondimensional parameter in the problem is:

$$\Upsilon \equiv 4\frac{\Psi f_0}{H_{\text{mix}}^2 N_{\text{mix}}^2}. \tag{5.6}$$

Υ is a measure of the strength of the geostrophic flow; specifically, $\Upsilon \sim \zeta_{\text{min}}/\Omega$ where $\Omega \sim \alpha^2 H_{\text{mix}}^2 N_{\text{mix}}^2/f_0$ is the back-rotated frequency of a wave whose horizontal scale is that of the geostrophic flow and whose vertical scale is the mixed layer depth.

The solution of the initial value problem is discussed mainly using dimensional variables. However, the considerations above show that there are only three independent nondimensional parameters, viz., μ, $\hat{H}$ and Υ. In fact, of the parameters in the barotropic streamfunction, Ψ and α, the length scale α^{-1} appears only in the time scale, T. Hence changes in the strength of background flow are made by modifying Ψ, which is equivalent to changing Υ.

b. The standard case

We now examine the temporal behavior of the solution for a particular selection of model parameters which we refer to as the 'standard' case (we use the label S to signify this case in subsequent figures); these choices are listed in Table 1. Figures 9–11 summarize the results; because $\Upsilon = 3.302$ (corresponding to a peak velocity of 10 cm s^{-1}), the standard case has a fairly strong background flow.

In Figure 9 we show how the 'speed,' $\sqrt{\overline{L\mathscr{A}L\mathscr{A}^*}} = \sqrt{\overline{u^2 + v^2}}$, evolves in time. Initially, the speed is sharply concentrated in, and just below, the mixed layer (see Fig. 6). But after 10 days (Fig. 9a), the development of both horizontal and vertical structure is evident.

In the mixed layer itself, the sinusoidal barotropic flow $(\psi, \zeta) \propto \cos 2\eta$ impresses an analogous modulation $\cos 2\eta$ on the NIO speed. In fact, the modulation is so strong that it increases the speed by about 20% over its initial value in the vicinity of the vorticity minima ($\eta = \pi/2$). The structure is very different directly below the mixed layer. Enhanced

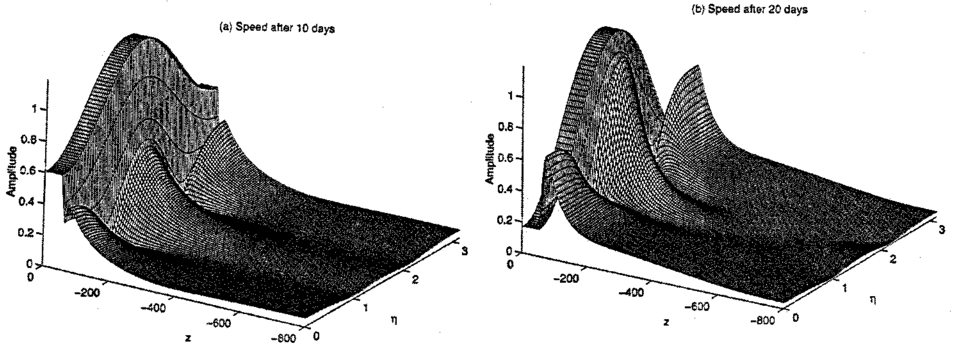

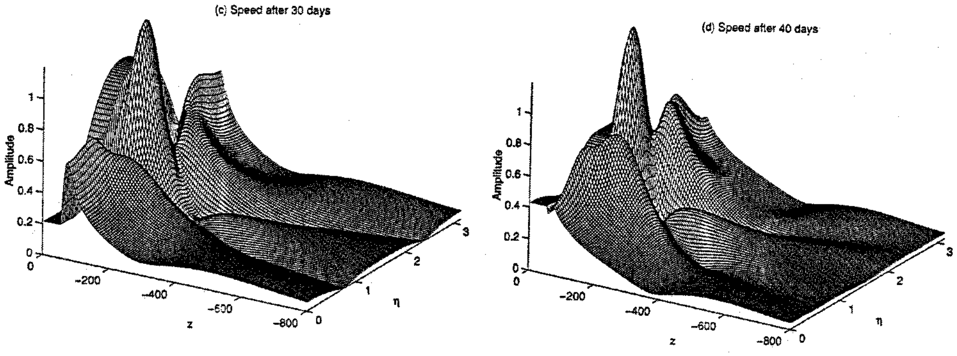

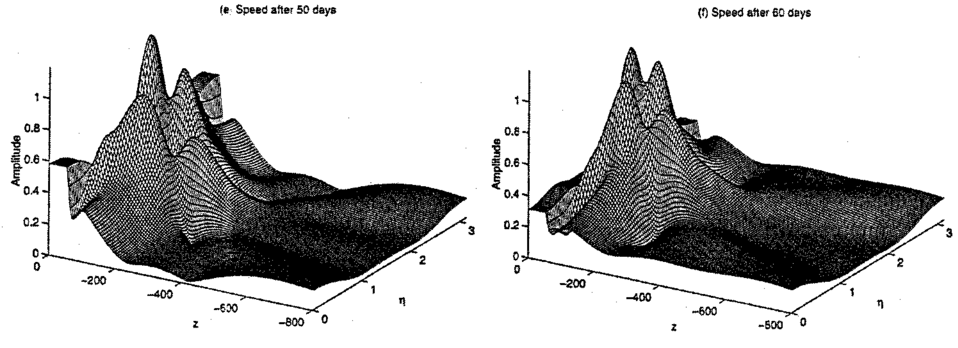

Figure 9. Panels (a)–(f) show snapshots of the speed, $|L\mathscr{A}(y, z, t)| = \sqrt{u^2 + v^2}$, as surface plots above the (η, z) plane every 10 days after the initiation of the near-inertial oscillation. The depth z is in meters and $\eta = 2\alpha y$ is dimensionless.

downward propagation is correlated with *both* the maxima and the minima of the vorticity; this results in a second harmonic, cos 4η, structure in the NIO speed below the mixed layer.

In some respects these patterns agree with the observations described by van Meurs (1998). First, the rate at which near-inertial activity 'disappears' from the mixed layer is spatially inhomogeneous; van Meurs observed that the time scale varied between 2 and 20 days depending on location. van Meurs also attempted to correlate the energy level with the geostrophic vorticity; Figure 9a suggests that *in the mixed layer* there is a strong correlation: high NIO energy with negative vorticity (e.g., $\eta = \pi/2$) and low NIO energy with positive vorticity (e.g. $\eta = 0$ and π). Such a correlation was not seen unambiguously in van Meurs's drifter observations. It may be that the mesoscale vorticity is not well resolved by this data set. Alternatively, if some of the drifters happened to be drogued to fluid beneath the mixed layer then those drifters would see elevated energy levels at both the maxima and minima of the vorticity (as in Fig. 9a).

By 20 days, the spatial pattern is even clearer (Fig. 9b). Notice that near the vorticity maxima ($\eta = 0$ and π) the speed now has a submixed-layer maximum. In other words, it appears as though the near-inertial energy has been expelled from the mixed layer at $\eta = 0$ and π and concentrated just below the base of the mixed layer. These concentrations of activity subsequently propagate horizontally (Figs. 9b–9e) and add to downwardly propagating oscillations from the mixed layer near $\eta = \pi/2$. This results in the formation of a substantial peak in speed just below the mixed layer at the vorticity minima ($\eta = \pi/2$).

Over this period, the activity in the mixed layer near the vorticity minimum begins to decline. Eventually, in Figures 9d–f, the near-inertial activity disperses downward. At the vorticity minimum ($\eta = \pi/2$), the mixed-layer speed finally falls below its initial level. By 60 days, activity remains peaked below the mixed layer at the vorticity minimum and very deep penetration of near-inertial activity takes place only in regions of positive vorticity (in Fig. 9f, near $\eta = 0$ and π, the speed is fairly uniform over the top 1000 m).

More quantitative features of the solution are shown in Figures 10 and 11. Figure 10 shows the backrotated velocity field below both the maximum (Fig. 10a) and the minimum (Fig. 10b) of the vorticity. The contours in Figure 10 are curves of constant speed. Both parts of Figure 10 show the formation of what D'Asaro *et al.* (1995) call a "beam." In Figure 10b, the "beam" is composed of strong inertial currents below the mixed layer, and is located roughly in the region between $z = -50$ m and $z = -100$ m. In fact, as the contour labelled 1.25 indicates, the speed can be larger than that of the initial condition. The "beam" is also apparent, though less intense, in Figure 10a.

Figure 11 shows the backrotated shear vectors below the maximum (Fig. 11a) and minimum (Fig. 11b) of the vorticity. Because the shear field is shallower, and has more small-scale structure than the velocity field, we have changed the depth scale relative to that of Figure 10. We have also not shown the mixed layer (where the shear is zero). There are interesting qualitative differences between Figure 11a and 11b. (The differences are greater than those between Figs. 10a and 10b.)

c. *Parametric variations*

As gross indications of how changes in the parameters alter the evolution, we use two averaged measures of the inertial activity in the mixed layer.

(a) Speed contours, backrotated velocity vectors at vorticity maximum

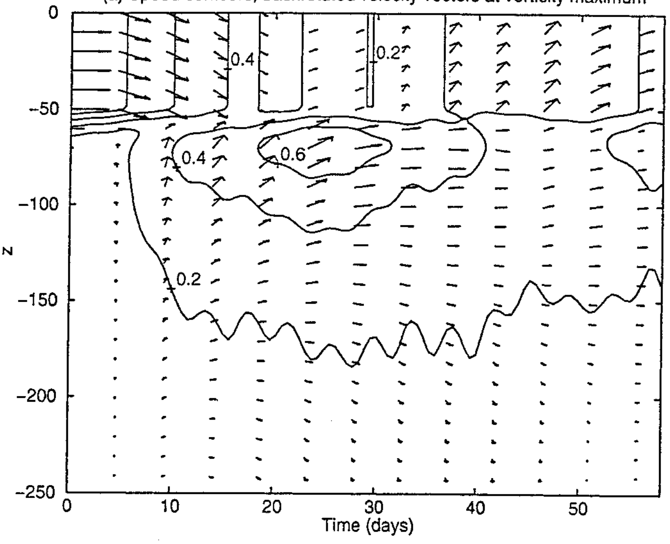

(b) Speed contours, backrotated velocity vectors at vorticity minimum

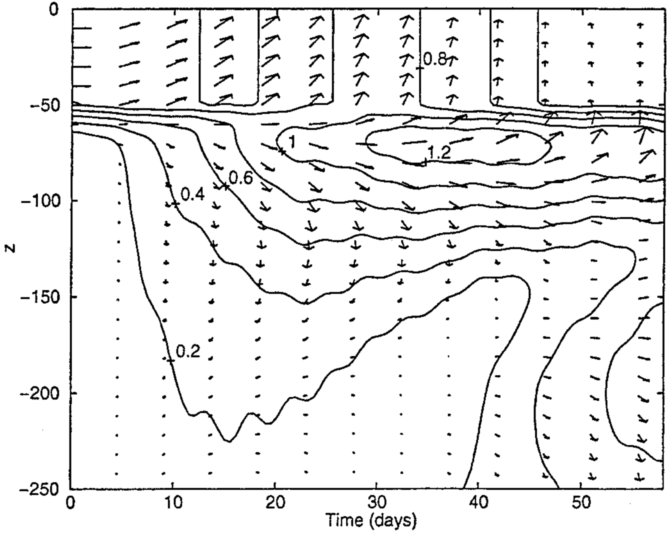

Figure 10. Temporal evolution of the backrotated velocity field (u, v), with depth z (meters) at (a) the vorticity maxima ($\eta = 0, \pi, \ldots$), and (b) the vorticity minima ($\eta = \pi/2, 3\pi/2, \ldots$). Shown are the backrotated velocity vectors at the points (t, z). The contours are curves of constant speed, $\sqrt{u^2 + v^2}$. The initial speed in the mixed layer is 1 and the contour interval is 0.2.

(a) RMS shear contours, backrotated shear vectors at vorticity maximum

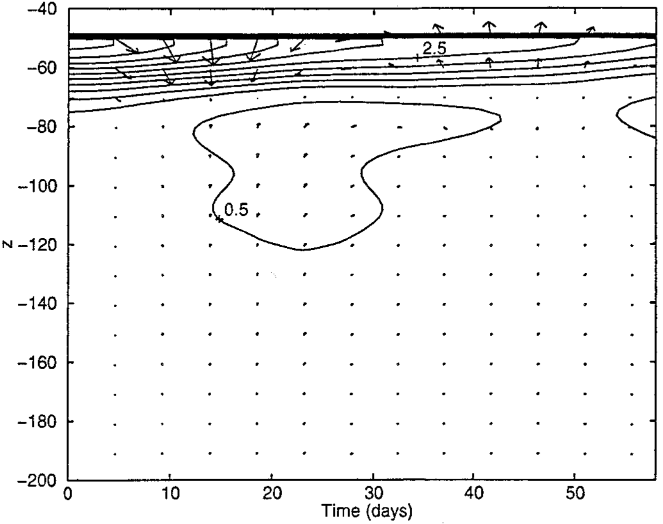

(b) RMS shear contours, backrotated shear vectors at vorticity minimum

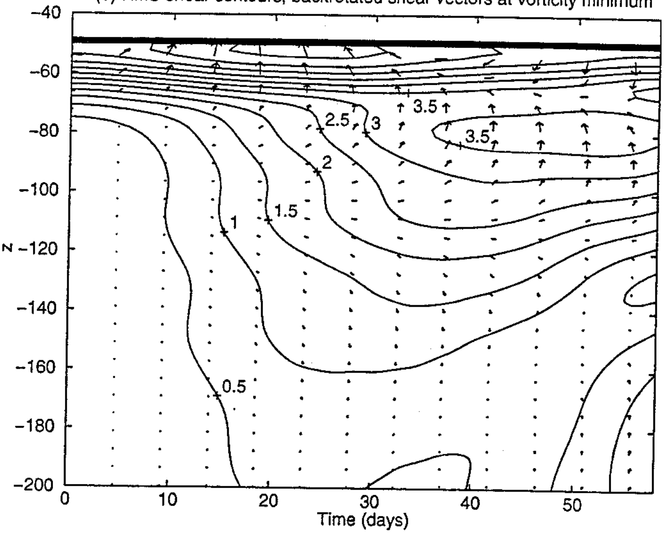

Figure 11. Temporal evolution of the backrotated shear field (u_z, v_z), with depth z (meters) at (a) the vorticity maxima ($\eta = 0, \pi, \ldots$), and (b) the vorticity minima ($\eta = \pi/2, 3\pi/2, \ldots$). Note: The depth scale in this figure differs from that of Figure 10. Shown are the backrotated shear vectors at the points (t, z). The contours are curves of constant shear strength, $\sqrt{u_z^2 + v_z^2}$. In the initial condition, the shear has a maximum value of 5.14.

First, from (3.11a) and (4.7), we obtain the horizontally averaged velocity,

$$\begin{aligned}\langle u + \mathrm{i}v\rangle &\equiv \frac{\alpha}{\pi}\int_0^{\pi/\alpha} (u + \mathrm{i}v)\,\mathrm{d}y,\\ &= \frac{1}{2\pi}\,e^{-\mathrm{i}f_0 t}\sum_{n=1}^{80}\sum_{r'=0}^{10} \epsilon_n\sigma_n \exp\left(-\mathrm{i}\omega_{2r',n}t\right)\,\Xi^2_{2r',n}\hat{p}_n(z).\end{aligned} \tag{5.7}$$

In the mixed layer, the expression above simplifies because $\hat{p}_n(z) = 1$. Thus, one measure of inertial activity, obtained from (5.7) with $\hat{p}_n = 1$, is the magnitude of the horizontally averaged mixed-layer velocity; that is, $\sqrt{\langle u\rangle^2 + \langle v\rangle^2}$.

Our second measure of near-inertial activity uses the shear: The horizontal average of the shear is, from (4.8),

$$\langle u_z + \mathrm{i}v_z\rangle = -\frac{1}{2\pi}\,e^{-\mathrm{i}f_0 t}N^2\sum_{n=1}^{80}\sum_{r'=0}^{10} \epsilon_n\sigma_n\Xi^2_{2r',n}\exp\left(-\mathrm{i}\omega_{2r',n}t\right)\,\hat{h}_n(z), \tag{5.8}$$

from which we may construct the magnitude $\sqrt{\langle u_z\rangle^2 + \langle v_z\rangle^2}$ at a depth of 51 m. This depth, one meter below the base of the model mixed layer, is very close to where the initial shear in Figure 6 achieves its maximum value.

Suppose that the parameters defining the sinusoidal flow in (3.1) are varied by changing both α and Ψ so that the timescale T in (5.2) is fixed at the value of the standard case, namely $T = 9.26$ days. Figure 12a then shows the decrease of $\sqrt{\langle u\rangle^2 + \langle v\rangle^2}$ versus $\hat{t} = t/T$ at five different values of Υ. Figure 12b shows the variation of $\sqrt{\langle u_z\rangle^2 + \langle v_z\rangle^2}$ at the base of the mixed layer in the same five cases. The trend in Figure 12 is clear: increasing Υ in (5.4), while holding $T = 2/|\zeta_{\min}|$ fixed enhances the decay of mixed-layer speed and shear (though the shear is less sensitive to changes in Υ than the speed).

The parameter Υ is the most important nondimensional group controlling the decay rate of inertial activity in the mixed layer; the results in Figure 12 are insensitive to changes in the other two nondimensional parameters, μ and $\hat{H}$, of (5.3). For example, for the parameter values summarized in Table 2, Υ and T are fixed, but the stratification parameters are altered by factors of over two. Figure 13 shows the decay of $\sqrt{\langle u\rangle^2 + \langle v\rangle^2}$ in these different cases; the decay is clearly similar for all four.[4]

The horizontal modulation of the NIO is also strongly dependent on changes in Υ. To illustrate this behavior, consider the three calculations in Figure 12a with $\Upsilon = 3.302, 1.651$ and 0.413 at the times when $\sqrt{\langle u\rangle^2 + \langle v\rangle^2} = 0.54$ in the mixed layer. For the standard case, this is at $t = 30$ days, or $t/T = 3.24$, and Figure 9c shows a snapshot of the speed, $\sqrt{u^2 + v^2}$,

---

[4] In view of the sensitivity in Figure 12, the collapse of the four curves in Figure 13 is impressive, but not perfect. The differences which remain in Figure 13 are due to two effects. The most important is that the filtering factor, $\exp(-n^2/600)$ in (4.3b), is not changed when the parameters are varied. Thus, in terms of the nondimensional coordinate $\hat{z}$ in (5.1), the four cases have slightly different initial conditions. Second, because of the large differences in $\hat{H}$, the lowest vertical modes have significantly different frequencies; this produces idiosyncratic 'wiggles,' such as the large dip on curve B at around $t/T = 8$.

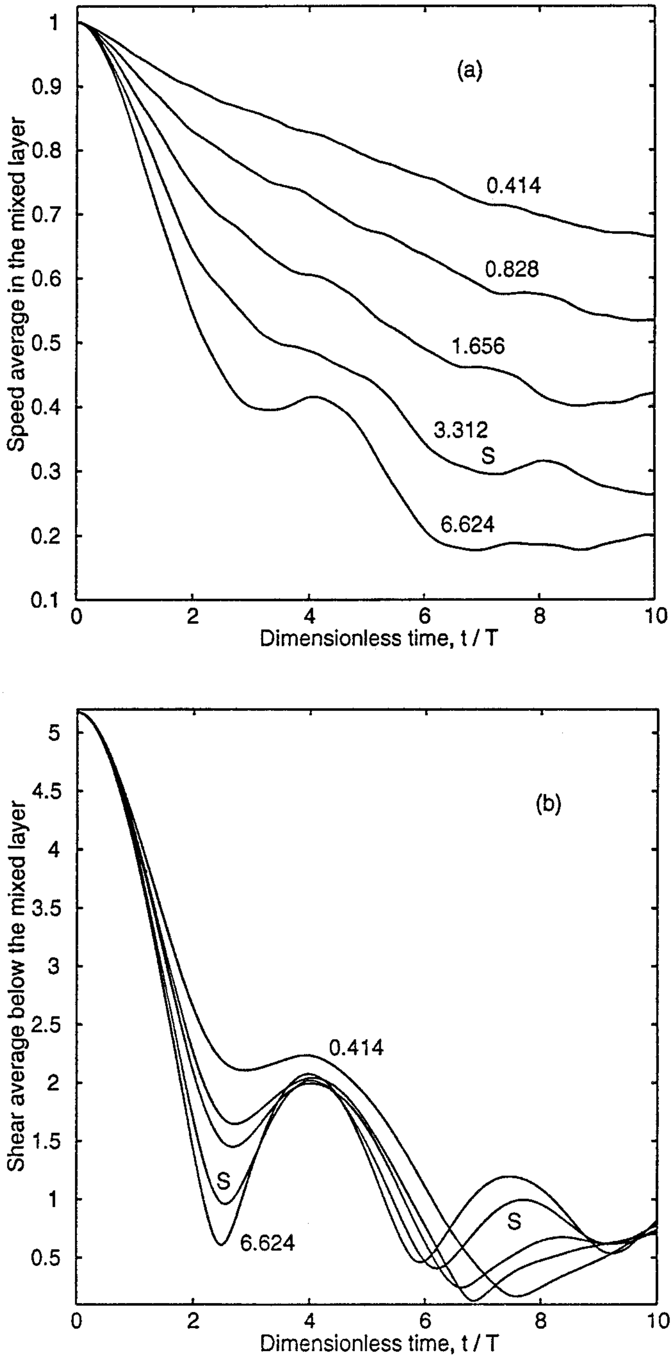

Figure 12. (a) Evolution of the speed, $\sqrt{\langle u\rangle^2 + \langle v\rangle^2}$, or the horizontally averaged velocity, $\langle u + \mathrm{i}v\rangle$ defined in (5.7). The value of Υ in the five different curves is indicated beside each curve. The case with $\Psi = 4000\ \mathrm{m}^2\ \mathrm{s}^{-1}$, or $\Upsilon = 3.302$, is the standard case shown in Figures 9 through 11. The horizontal axis is in units of t/T where $T \equiv 1/(2\alpha^2\Psi)$. (b) Temporal evolution of the magnitude of the shear of the horizontally averaged flow, $\sqrt{\langle u_z\rangle^2 + \langle v_z\rangle^2}$.

Table 2. Four parameter settings, all with $\Upsilon \equiv 4\Psi/f_0/(N_{\mathrm{mix}}H_{\mathrm{mix}})^2 = 3.302$ and all with the same timescale, $T = 1/(2\alpha^2\Psi) = 9.26$ days. S denotes the standard case from Table 1. The buoyancy profile is specified by giving $(H, H_{\mathrm{mix}}, z_0, N_{\mathrm{mix}})$ and then the stratification parameter, s in (4.1), is calculated from $s = N_{\mathrm{mix}}[z_0 - H + H_{\mathrm{mix}}]$. In all four cases $H = 4200$ m and $z_0 = 4329.6$ m.

Case	Ψ ($\mathrm{m^2\,s^{-1}}$)	α^{-1} (km)	N_{mix} ($\mathrm{s^{-1}}$)	H_{mix} (m)	μ	$\hat{H}$	s ($\mathrm{m\,s^{-1}}$)
S	4000	80	0.01392	50	0.1392	83	2.5000
A	1000	40	0.01392	25	0.0808	167	2.1520
B	1000	40	0.009843	35.35	0.1071	117.8	1.6236
C	4000	80	0.006960	100	0.2178	41	1.5980

as a surface plot above the (η, z) plane. Figure 14 shows the analogous surface plots for the other two calculations with smaller values of Υ. As Υ is reduced the horizontal modulation of the NIO fields become weaker. (The strong dispersion approximation of Young and Ben Jelloul (1997) is valid in the case $\Upsilon \ll 1$; the leading order term of this approximation is that $\mathscr{A}$ is independent of the horizontal coordinates. Figure 14b is approaching this weakly modulated state.)

d. Radiation of a near-inertial wave train

In the standard case, the solution develops what we have termed a "beam" (following D'Asaro *et al.*, 1995). This is the shallow concentration of energy which first appears

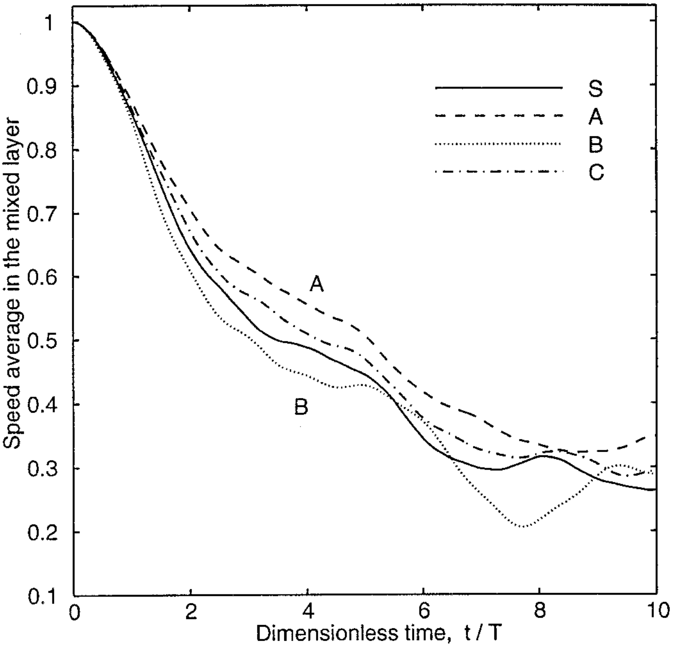

Figure 13. Evolution of the speed, $\sqrt{\langle u\rangle^2 + \langle v\rangle^2}$, for the four parameter sets (A, B, C and S) in Table 2. $\Upsilon = 3.302$ in all cases, while μ and $\hat{H}$ have large variations.

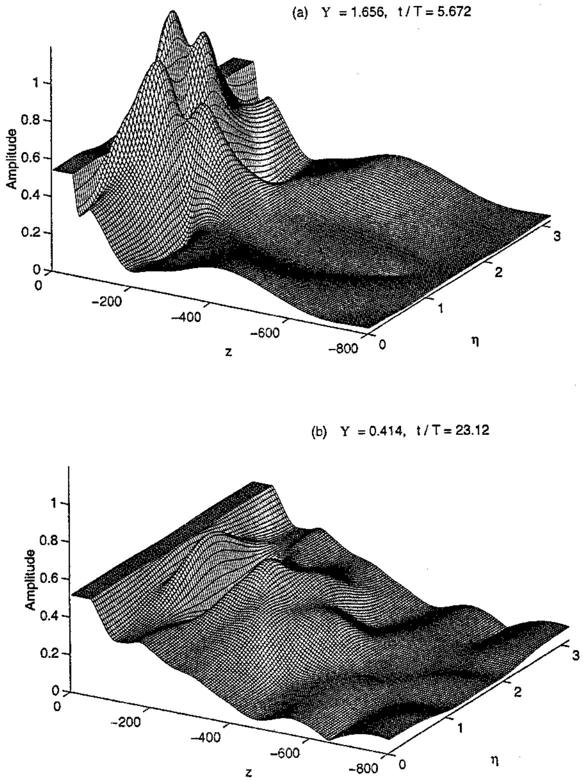

Figure 14. Snapshots of the speed, $|L\mathscr{A}(y, z, t)| = \sqrt{u^2 + v^2}$, as a surface plot above the (η, z) plane. The two calculations above, and the one in Figure 9c, all have $\sqrt{\langle u\rangle^2 + \langle v\rangle^2} = 0.54$ in the mixed layer. The value of Υ and the nondimensional time is indicated on the figure. As Υ is increased, the horizontal structure of the fields becomes more complex. When Υ is small, as in Figure 14b, the relatively weak horizonal modulations indicate that the strong dispersion approximation of Section 6 is valid.

below the base of the mixed layer at the vorticity maximum and then moves horizontally to the vorticity minimum (see Fig. 9). We stress that the vertical propagation of the beam is modest; the maximum in near-inertial energy is concentrated just below the base of the mixed layer (see Fig. 10). The phenomenon occurs at depth between 50 and 100 m.

Another interesting phenomenon, which occurs at a different parameter settings (namely, when $0.3 \le \Upsilon \le 1$), is illustrated in Figure 15: a train of near-inertial waves is radiated from the mixed layer into the deeper ocean. Because the train is confined to the neighborhood of vorticity minimum, it has a relatively small horizontal length scale. In contrast to the beam, the near-inertial wavetrain has a substantial vertical propagation.

The wavetrain is evidently a phenomenon in which the modes of the system are acting in concert to produce local, vertically propagating wave packets. In fact, the horizontal localization of the train near the vorticity minimum is explained by Kunze's ray-tracing

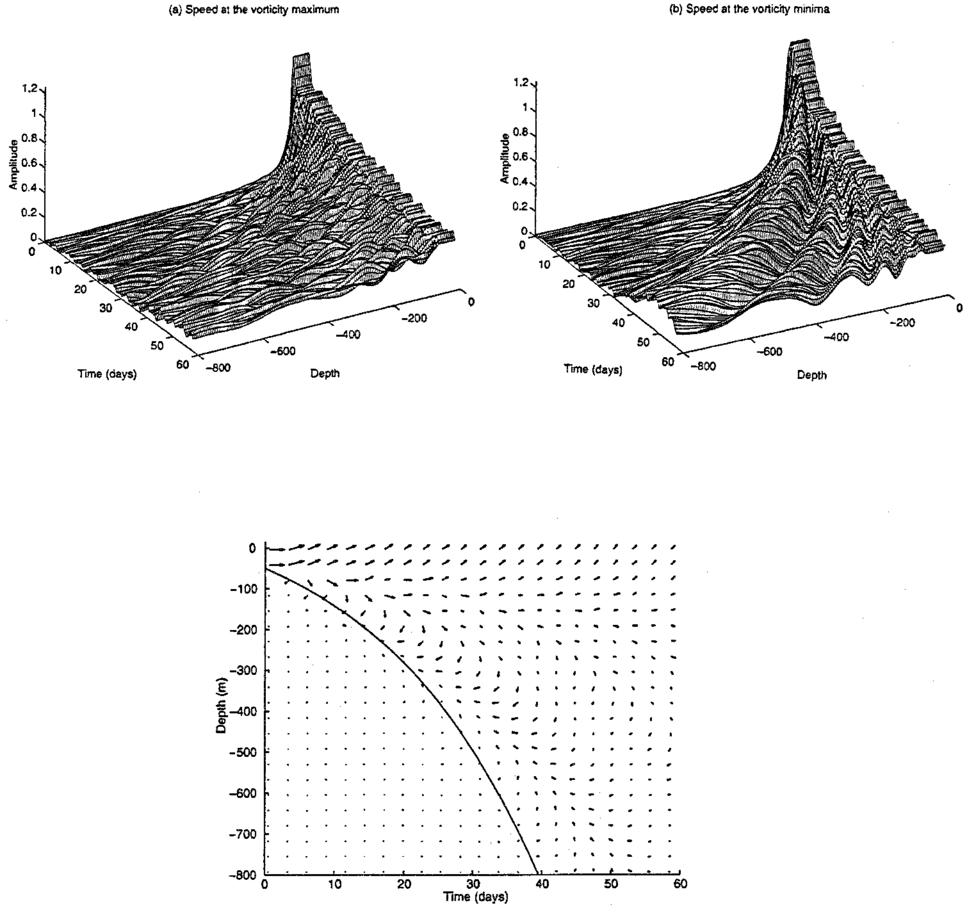

Figure 15. An illustration of the radiation of a near-inertial wave train from the mixed layer. (a) Speed as a function of depth (meters) and time (days) below the vorticity maxima, $\eta = 0$ and π. (b) Speed as a function of depth and time below the vorticity minima, $\eta = \pi/2$. The wave train is apparent only below the vorticity minimum. (c) Another view of the near-inertial activity below the vorticity minimum; the arrows indicate the backrotated velocity, $L\mathscr{A} = \exp(if_0t)(u + iv)$, superposed on a depth-time plot. The solid curve is the trajectory in (5.12). Notice the reversal in direction with depth of the near-inertial velocity.

arguments. Equivalently, the Mathieu modes of Figures 1 and 2 tend to be trapped around the vorticity minimum at $\eta = \pi/2$. More precisely, from the Mathieu equation (3.3), there are turning points at the values of η determined by $a - 2q \cos 2\eta = 0$, or equivalently $2\omega = \zeta_{\min} \cos 2\eta$. In the vicinity of the vorticity minimum bounded by these points, waves may propagate vertically; they are evanescent elsewhere. This explains qualitatively why the wavetrain arises at the vorticity minimum and not at the maximum.

A second argument follows from considering an effective group velocity. Because most

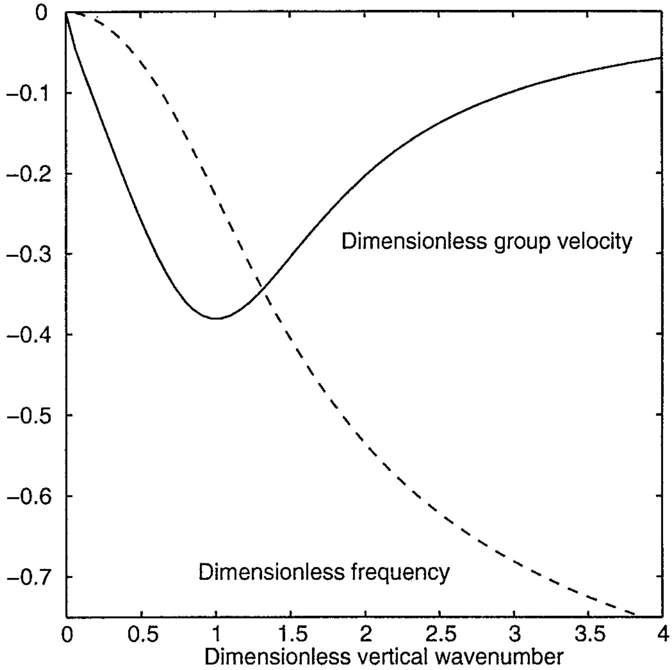

Figure 16. The dimensionless frequency $\hat{\omega}$ (the dashed curve) in (3.8b) as a function of the dimensionless vertical wavenumber, $\hat{m}$ in (3.8a). Only the $r = 0$ branch from Figure 3 is shown. Also shown is the dimensionless vertical group velocity $\hat{\omega}_{\hat{m}}$ (the solid curve). The vertical group velocity has an extremum at around $\hat{m} = 1.0$.

of the energy is contained in the Mathieu mode with $r = 0$, we use the nondimensional dispersion relation in (3.9) and consider only the zeroth eigenmode. Figure 16 shows the nondimensional frequency and group velocity,

$$\hat{\omega} = a_0(\hat{m}^2)/2\hat{m}^2 \qquad \text{and} \qquad \hat{\omega}_{\hat{m}} = [\hat{m}^{-1}a_0'(\hat{m}^2) - \hat{m}^{-3}a_0(\hat{m}^2)], \tag{5.9a,b}$$

as functions of $\hat{m}$. The crucial point is that the group velocity has a minimum (i.e., most negative) value at $\hat{m}_* \simeq 1.0$. In terms of dimensional variables, the extremum is at

$$m_* \simeq \sqrt{N^2/2\Psi f_0}, \tag{5.10a}$$

and the minimum group velocity is

$$c_{g*} \simeq -0.38\alpha^2\Psi\sqrt{\frac{2\Psi f_0}{N^2}}; \tag{5.10b}$$

the frequency at $m = m_*$ is

$$\omega_* \simeq -0.24\alpha^2\Psi. \tag{5.10c}$$

As an application of these results one can calculate the position of the front of the wavetrain in Figure 15 by integrating

$$\frac{\mathrm{d}z}{\mathrm{d}t} = c_{g*}(z), \tag{5.11}$$

where the dependence of c_{g*} on z arises because $N(z)$ is given by (4.1). On using the initial condition $z(0) = -H_{\mathrm{mix}}$, one finds that

$$z(t) = (z_0 - H) + (H - H_{\mathrm{mix}} - z_0) \exp\,[0.38\alpha^2(2\Psi)^{3/2} f_0^{1/2} s^{-1} t]. \tag{5.12}$$

The trajectory in (5.12) is plotted in Figure 15c and gives an indication of the location of the front of the wavetrain.

It is interesting that the vertical group velocity in (5.10b) is proportional to N^{-1}. This explains the acceleration with depth of the front of the wavetrain in Figure 15c (the front goes faster as N decreases). The standard internal wave dispersion relation has the opposite tendency: with fixed k and m the vertical group velocity of internal waves in a resting ocean ($\Psi = 0$) decreases as N decreases.

Wavetrains like that of Figure 15 occur only if Υ is neither too small nor too large. Roughly speaking, if $N(z)$ is specified using the parameters in Table 1, then trains are prominent over the range, $0.3 \leq \Upsilon \leq 1$. To rationalize this dependence on Υ, notice that if $\Upsilon \propto \Psi \rightarrow 0$, then the wavenumber m_* in (5.10a) becomes large; the maximum group velocity occurs at high vertical wavenumbers which are not initially excited. On the other hand, if $\Upsilon \gg 1$ then m_* becomes small; the maximum group velocity approaches small vertical mode numbers and eventually, certainly before $m_*^{-1} \sim H$, there is no longer an effective continuum of modes. In this case the concept of a group velocity is meaningless, and in numerical calculations, we observe little coherent vertical propagation, but rather substantial horizontal modulation.

6. Limiting cases

Throughout this paper we have confined attention to the sinusoidal flow in (3.1). This narrow focus has enabled us to obtain a detailed picture of the radiation of a large-scale, near-inertial excitation. Now we consider two limiting cases, $\Upsilon \ll 1$ and $\Upsilon \gg 1$, in which insight can be obtained by analytical considerations.

a. Strong dispersion: $\Upsilon \ll 1$

The case $\Upsilon \ll 1$ corresponds to the strong dispersion approximation of Young and Ben Jelloul (1997). The validity of strong dispersion requires $\Psi/f_0R_n^2 \ll 1$. For the low modes, with $R_n > 10$ km, $\Psi/f_0R_n^2$ is small. But because $R_n \rightarrow 0$ as n increases, the strong dispersion approximation fails for sufficiently high vertical modes. We can better appreciate the utility of the approximation by applying it to the specific problem we have solved in this paper.

In the present context, the strong dispersion approximation is a perturbative solution of the nondimensional $\mathscr{A}$-equation (5.5) in the case $\Upsilon \ll 1$. By expanding $\mathscr{A} = \mathscr{A}_0 + \Upsilon \mathscr{A}_1 + \cdots$, one finds that the leading order is just $\mathscr{A}_{0\eta\eta} = 0$; that is, horizontal wave dispersion dominates. The solution of the leading order problem is therefore

$$\mathscr{A}_0 = \mathscr{A}_0(z, t). \tag{6.1a}$$

In Appendix B the expansion is carried to higher order; the final result, in dimensional variables, is an evolution equation for $\mathscr{B} \equiv L\mathscr{A}_0$:

$$\mathscr{B}_t + \mathrm{i} f_0^{-1} K L \mathscr{B} = 0, \tag{6.1b}$$

where $K \equiv \alpha^2\Psi^2$ is the average kinetic energy density of the sinusoidal flow (3.1). The dispersion relation obtained from (6.1b) is the parabola, $\hat{\omega} = -\hat{m}^2/4$, labelled 'SDA' in Figure 3.

In the strong dispersion approximation, the small parameter, Υ, multiplies the terms with the most z-derivatives in (5.5); this hints that the expansion in (6.1) is not uniformly valid for the high vertical modes. This nonuniformity can be assessed more precisely by returning to the horizontal eigenproblem, the Mathieu equation in (3.3a), and noting that the strong dispersion approximation is equivalent to using the $q \ll 1$ expansion of the $r = 0$ eigenfunction, i.e.

$$ce(\eta, q) = \frac{1}{\sqrt{2}}\left[1 - \frac{q}{2}\cos 2\eta + O(q^2)\right]. \tag{6.2}$$

On referring to Figure 1a, we see that if $q \ll 1$ then the eigenmodes have weak horizontal modulation. But because $q \equiv 2\Psi/\hbar_n \sim n^2$ (see Fig. 5), the expansion is invalid as $n \to \infty$ with Ψ fixed.

Because the strong dispersion approximation fails for sufficiently high vertical mode number, n, its validity is determined by how strongly the initial condition excites modes with $n \gg 1$. Moreover, the strong dispersion approximation filters all of the horizontal modes with $r \geq 2$. Hence we also require a weak excitation of these more complicated horizontal structures.

We make a pragmatic assessment of the approximation by tolerating a fractional, frequency error of about 0.3. That is, referring to Figure 3, let us say that the strong dispersion approximation is acceptable if

$$q = \hat{m}^2 < 2. \tag{6.3}$$

(Because $a_0(2) = 1.51395$, the error in the SDA eigenfrequency is 32% at $q = 2$.) Given (6.3), and the definition $q \equiv 2\Psi/f_0R_n^2$, we can plot the curve $\Psi = f_0R_n^2$ (equivalently $q = 2$) in the (n, Ψ) plane; see Figure 17. In the region below the curve, we decree that the approximation is acceptable.

Also superposed on Figure 17 is the cumulative fraction of energy which is contained in modes with vertical mode number less than or equal to n. That is, because $\sigma_n\epsilon_n^2$ is the

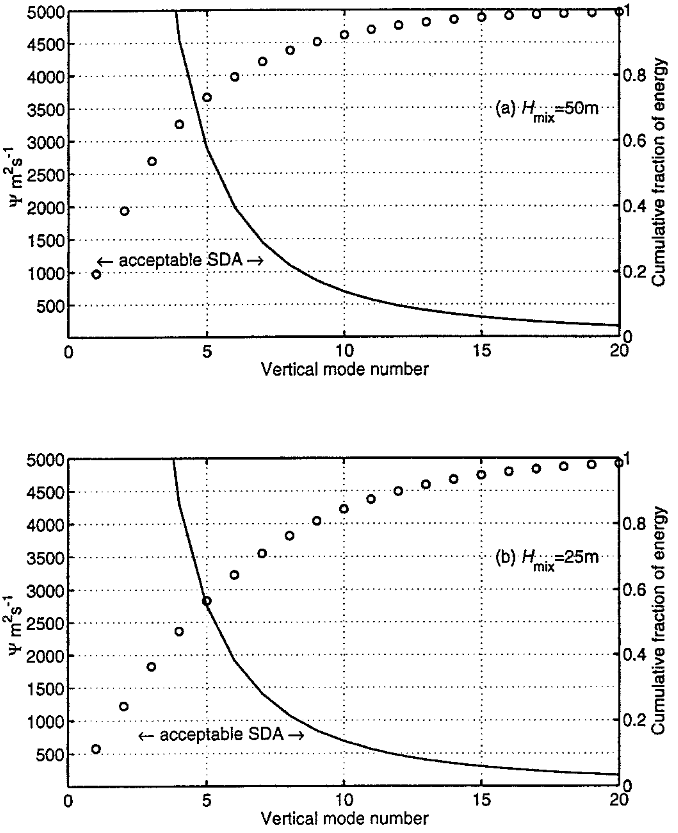

Figure 17. The figure above can be used to estimate the fraction of the energy which is contained in modes which are acceptably described by the strong dispersion approximations. The solid curve is $q = 2$ (that is, $\Psi = f_0 \hbar_n^2$) as a function of the vertical mode number, n. This curve depends on the parameters used to specify the model buoyancy profile in (4.1); shown above are two examples with different values of $H_{\rm mix}$ as indicated. (The other parameters are given in Table 1.) The circles and right-hand ordinate show the cumulative fraction of energy contained in modes with vertical mode number less than or equal to n.

fraction of energy in vertical mode number n, the right-hand axis shows

$$C_n \equiv \sum_{j=1}^{n} \epsilon_n^2 \sigma_n, \tag{6.4}$$

as a function of n. The two parts of Figure 17 are for different values of $H_{\rm mix}$.

Given the value of Ψ, we read off the number of modes that are acceptably approximated by strong dispersion, and also the amount of energy contained in them. For example, with $\Psi = 2000$ m^2 s^{-1}, the accurately approximated modes are those with $n \leq 6$. These modes contain 80% of the energy if $H_{\rm mix} = 50$ m, but only 65% if $H_{\rm mix} = 25$ m. Provided that the

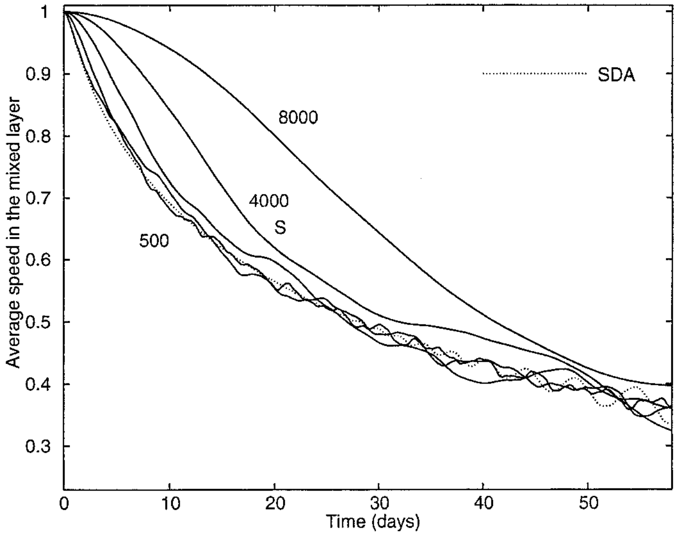

Figure 18. Comparison of the speed of the average velocity in the mixed layer (defined in (5.7) with $\hat{p}_n(z) = 1$) calculated with the strong dispersion approximation (6.5) with that obtained from the full series expansion in (4.8). The results from (4.8) are the solid curves and the standard case from Table 1 is labelled 'S'. The other four solid curves are obtained by varying Ψ by factors of 2 with the kinetic energy density, $K = \alpha^2\Psi^2$, fixed. The value of Ψ is indicated in three cases; e.g. for the standard case, $\Psi = 4000\ \mathrm{m}^2\ \mathrm{s}^{-1}$. The approximation (6.5) is the dotted curve.

fraction of energy contained in these "strongly dispersing" modes is sufficiently large, we have some grounds for making the approximation. Accordingly, we might expect the approximation to be adequate in the former example, less so in the latter.

Hence, if we insist that 80% of the energy must be contained in the strongly dispersing modes in order to use the approximation, then this restricts us to the parameter regime $\Psi < 2000\ \mathrm{m}^2\ \mathrm{s}^{-1}$ if $H_{\mathrm{mix}} = 50$. This range is sufficiently wide to make the approximation a relatively useful tool in more complicated situations.

As an example of the application of the approximation, the solution of (6.1b) with the initial condition in Figure 6, is

$$L\mathscr{A}_0 = \sum_{n=1}^{80} \sigma_n \epsilon_n \hat{p}_n(z) \exp\left(\mathrm{i}\frac{Kt}{\hbar_n} \right). \qquad (6.5)$$

Figure 18 shows a comparison between the approximate solution in (6.5) (the dotted curve) and the full numerical solutions. The standard case, which has $\Upsilon = 3.302$ is labelled by 'S'. The other solid curves in Figure 18 are obtained by varying Ψ, and therefore Υ, by factors of 2 while also adjusting α so that the kinetic energy density, $K = \alpha^2\Psi^2$ is fixed. Figure 18 shows that the standard case is not well approximated by (6.5), but that if $\Upsilon = 1.651$ ($\Psi = 2000$) is less, there is agreement.

One interesting point, apparent from (6.5), from Figure 18 and also from the multiple time scale expansion in Appendix B, is that in the strong dispersion regime the relevant evolutionary time scale is

$$\frac{T}{\Upsilon} = \frac{1}{8}\frac{N_{\text{mix}}^2 H_{\text{mix}}^2}{f_0 K}. \tag{6.6}$$

Notice that T/Υ depends only on the combination $K = \Psi^2\alpha^2$ (not on Ψ and α separately). This explains the condensation of the solid curves in Figure 18 as Υ is reduced with K fixed: once one enters the strong dispersion regime the rate of decay of mixed layer speed is insensitive to further reductions in Υ.

b. Strong trapping: $\Upsilon \gg 1$

When Υ is large we may again simplify (5.4) by asymptotic means. We proceed by defining a small parameter, $\epsilon = \Upsilon^{-1/4}$. Next, we observe that for a fixed mixed layer structure (constant H_{mix} and N_{mix}), $q \propto \Upsilon$ where q is the Mathieu parameter in (3.3). Hence in this limit, $q \gg 1$, and the Mathieu modes into which we decompose the initial condition are localized (or 'strongly trappped') near the vorticity minimum at $\eta = \pi/2$ (see Section 3 and Fig. 1). This guides us to introduce a rescaling of the horizontal spatial coordinate:

$$\eta = \frac{\pi}{2} + \epsilon\xi, \tag{6.7}$$

We further define multiple timescales such that

$$\partial_t \rightarrow \partial_t + \epsilon^2\partial_\tau. \tag{6.8}$$

The governing equation is then

$$\hat{L}\mathscr{A}_t + \epsilon^2\hat{L}A_\tau + \mathrm{i}\cos(\pi + 2\epsilon\xi)\,\hat{L}\mathscr{A} + \mathrm{i}\epsilon^2\mathscr{A}_{\xi\xi} = 0. \tag{6.9}$$

On introducing the asymptotic sequence, $\mathscr{A} = \mathscr{A}_0 + \varepsilon\mathscr{A}_1 + \ldots$, we find, at leading order,

$$\hat{L}\mathscr{A}_{0t} - \mathrm{i}\hat{L}\mathscr{A}_0 = 0. \tag{6.10}$$

Without loss of generality, we solve (6.10) with

$$\mathscr{A}_0 = e^{\mathrm{i}t}\,\mathscr{C}(\eta, z, \tau), \tag{6.11}$$

where $\mathscr{C}$ is an as yet undetermined function.

The physical content of (6.11) is that at leading order the wave frequency is shifted by $\zeta_{\text{min}}/2$; indeed, because the modes are strongly trapped, Kunze's ray tracing approximation is applicable in this limit. However the small parameter in this approximation is $\epsilon = \Upsilon^{-1/4}$ and because of the small power it is difficult to access this asymptotic regime with oceanic values.

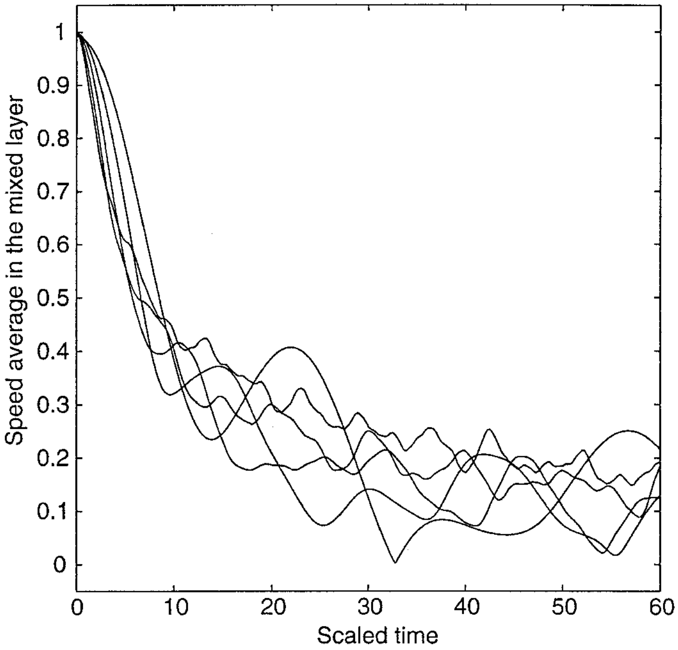

Figure 19. Speed averaged in the mixed layer against the scaled time t/T_1 where T_1 is defined in (6.14) for five calculations with $\Upsilon = 1.651, 3.302, 6.604, 13.21$ and 26.42. H_{mix} and N_{mix} are as in the standard case.

At order ϵ^2, we obtain

$$\hat{L}\mathscr{A}_{1t} - \mathrm{i}\hat{L}\mathscr{A}_1 + \hat{L}A_{0\tau} + \mathrm{i}\frac{\xi^2}{2}\hat{L}\mathscr{A}_0 + \mathrm{i}\mathscr{A}_{0\xi\xi} = 0. \tag{6.12}$$

The terms in $\mathscr{A}_1$ will lead to secularly growing solutions on the fast timescale t unless the terms containing $\mathscr{A}_0$ cancel. This leads to

$$\hat{L}C_\tau + \mathrm{i}\frac{\xi^2}{2}\hat{L}\mathscr{C} + \mathrm{i}\mathscr{C}_{\xi\xi} = 0. \tag{6.13}$$

The vertical transmission of the disturbance is therefore described by the solvability condition (6.13). That is, vertical propagation occurs on the timescale $\tau = t/\sqrt{\Upsilon}$. On restoring the dimensions, the dimensional timescale is

$$T_1 = \Upsilon^{-1/2}T \equiv \frac{H_{\mathrm{mix}}N_{\mathrm{mix}}}{4\alpha^2\Psi^{3/2}f_0^{1/2}}. \tag{6.14}$$

Evidently, the larger the Υ, the smaller the T_1, and so the energy disperses faster out of the mixed layer as one increases the strength of the geostrophic flow.

In Figure 19 we display the speed average in the mixed layer, plotted against the scaled time, t/T_1, for various values of $\Upsilon > 1$. Relative to Figure 12, the curves collapse rather more closely to a common behavior; we take this as confirmation that the dominant decay timescale is T_1 when $\Upsilon \gg 1$.

7. Discussion and conclusion

In this paper, we have given a detailed solution of an idealized problem which models the vertical transmission of near-inertial activity. Despite the many simplifications the model does represent some realistic features. For instance, in response to the questions posed in the introduction, the solutions show the way in which a pre-existing geostrophic flow creates horizontal modulations in an initially uniform NIO (e.g., Fig. 9). The solutions also show the formation of a 'beam' of near-inertial energy below the mixed-layer (cf. D'Asaro *et al.,* 1995).

Given these qualitative successes, in this conclusive section, a quantitative comparison of our results with observations, such as the Ocean Storms Experiment (D'Asaro *et al.,* 1995), is in order. However, such a comparison is not straightforward. One issue which has focussed research in this area for many years is the rate at which near-inertial activity disappears from the mixed layer after impulsive excitation. The model shows that the relevant time-scale depends on the value of the nondimensional group Υ in (5.4). The strong dependence of Υ on the spatially variable and subjectively determined parameters, H_{mix} and N_{mix}, makes decisive conclusions difficult.

Setting aside the problem of determining H_{mix} and N_{mix}, it is next necessary to appreciate some of the caveats of our model. We assume a simple, steady, barotropic flow, and consider linear, near-inertial oscillations; we restrict attention to two-dimensional flows, and ignore the effect of β. Even within the limited arena of idealized two-dimensional problems, we have used a streamfunction with a single sinusoid, which has the unrealistic feature that the wavenumber which contains all the energy is also the wavenumber containing all the vorticity.

Given all these lacunae, we can hope for no more than order of magnitude agreement between our model and observations. Nonetheless, we now attempt a comparison with Ocean Storms. First, we must assign "observational values" to Ψ and α of the model streamfunction, $\psi = -\Psi \cos(2\alpha y)$. D'Asaro *et al.* state that most of the kinetic energy is contained in features with approximately the Rossby radius scale; that is, 40 km. Accordingly we take

$$2\alpha = \frac{1}{40\ \text{km}}. \tag{7.1}$$

D'Asaro *et al.* also state that the RMS eddy velocity is $U_{RMS} = 0.053\ \text{m}^2\ \text{s}^{-1}$. Thus, from $\alpha\Psi = U_{RMS}/\sqrt{2}$, we obtain

$$\Psi = 3000\ \text{m}^2\ \text{s}^{-1}. \tag{7.2}$$

Given Ψ and α, we can now determine the minimum vorticity and the time scale $T = 2/|\zeta_{\min}|$ in the model:

$$\zeta_{\min} = 1.874 \times 10^{-6}\ \mathrm{s}^{-1}, \qquad T = 12.35\ \text{days}. \tag{7.3a,b}$$

To estimate Υ, we take $H_{\text{mix}} = 30$ m and $N_{\text{mix}} = 0.012\ \mathrm{s}^{-1}$ and we then find $\Upsilon = 10$. Hence, from Figure 12a, we estimate that to reduce the average speed to 0.3 of its initial level (that is, the energy to 10% of its initial level) one must wait for around $t = 3T$, or 37 days. This timescale is rather long, but there are greater uncertainties in both the model and the observational parameters.

For example, in calculating the model parameters above, we are led to an unavoidable inconsistency with the observations. The observed eddy vorticity has an RMS value of $0.023f \approx 2.46 \times 10^{-6}\ \mathrm{s}^{-1}$ and the observed $|\zeta_{\min}|$ is greater by a factor of three than the observed RMS vorticity. The model evidently does not have enough adjustable parameters to fit the observed spatial scales, the kinetic energy level, the RMS vorticity and the minimum vorticity. To determine roughly how much the failure of the model may affect our predictions, we calculate T directly from the observed vorticity: $\zeta_{\min} \approx 7.2 \times 10^{-6}$. This gives $T \approx 3.2$ days—shorter by a factor of 4 than (7.3b). If we further take the value (7.2) for Ψ, we find that the mixed layer energy falls to within 10% of its initial level after only 9.6 days, which is well within the observational constraints. In view of the many deficiencies of the model, we therefore regard our study as an encouraging success.

Acknowledgments. This research was supported by the National Science Foundation (Grant OCE-9616017). NJB thanks the Green Foundation for generous support. SGLS is a grateful recipient of a Lindemann Trust Fellowship.

APPENDIX A

Near-inertial waves with $k = 0$

The primitive equations for zonally-uniform disturbances on a unidirectional barotropic flow, with streamfunction $\psi(y)$ and vorticity $\zeta = \psi_{yy}$, are

$$\begin{gathered} u_t + f_e v = 0, \qquad v_t - fu + p_y = 0, \qquad p_z - b = 0, \\ v_y + w_z = 0, \qquad b_t + wN^2 = 0, \end{gathered} \tag{A1a–e}$$

where

$$f = f_0 + \beta y, \qquad f_e \equiv f_0 + \beta y + \zeta. \tag{A2}$$

One can eliminate all variables in favor of v to obtain

$$Lv_{tt} + ff_e Lv + f_0^2 v_{yy} = 0, \tag{A3}$$

where L is the differential operator in (2.2). By projecting (A3) on the vertical normal modes in (2.4), we find the Klein-Gordon equation,

$$v_{ntt} + ff_e v_n - c_n^2 v_{nyy} = 0, \tag{A4}$$

where $c_n = f_0 R_n$ is the modal speed.

If $\beta = 0$, and $\psi(y)$ is the sinusoid in (3.1), then we can look for horizontal modes by introducing

$$v_n(y, t) = V_n(y) \exp\left[-\mathrm{i}(f_0 + \omega)t\right]. \tag{A5}$$

The result is the Mathieu equation,

$$\frac{\mathrm{d}^2 V_n}{\mathrm{d}\eta^2} + (a - 2q \cos 2\eta)V_n = 0, \tag{A6}$$

where $\eta = \alpha y$ and

$$a = 2\left[1 + \frac{\omega}{2f_0}\right]\frac{\omega}{\hbar_n \alpha^2}, \qquad q \equiv 2\Psi/\hbar_n. \tag{A7a,b}$$

On comparing (A6) with the result obtained by setting $k = 0$ in (3.3) we see that the two expressions for a differ only because of the factor $1 + (\omega/2f_0)$. This factor is very close to unity for near-inertial oscillations (by definition). Setting the tautology aside, this calculations shows us how to make an *a posteriori* assessment of the validity of (2.11) (the eigenproblem which was derived by starting with Young and Ben Jelloul's NIO equation): one must check that $\omega/f_0 \ll 1$ for the most excited modes (this is indeed the case for the calculations presented in the main body of the paper).

The main point to note is that the NIO equation does not assume a spatial scale separation between the geostrophic flow and the near-inertial eigenmodes. Moreover, for the $k = 0$ modes, it is clear that our normal mode solution can be taken through even without the asymptotic scheme of Young and Ben Jelloul, and with negligible differences in the results.

APPENDIX B

The strong dispersion approximation

A specialized form of the strong dispersion approximation can be obtained by reducing (5.5) with $\Upsilon \ll 1$. On introducing the slow time

$$\tau = \Upsilon \hat{t}, \tag{B1}$$

we find

$$\Upsilon^2 \hat{L} \mathscr{A}_\tau + \Upsilon \mathrm{i} \cos 2\eta \, \hat{L} \mathscr{A} + \mathrm{i} \mathscr{A}_{\eta\eta} = 0. \tag{B2}$$

Now substitute $\mathscr{A} = \mathscr{A}_0 + \Upsilon \mathscr{A}_1 + \ldots$ into (B2). The terms of order Υ^0 are simply $\mathscr{A}_{0\eta\eta} = 0$, and thus $\mathscr{A}_0 = \mathscr{A}_0(z, t)$. The terms of order Υ^1 are

$$\mathrm{i} \cos 2\eta \, \hat{L} \mathscr{A}_0 + \mathrm{i} \mathscr{A}_{\eta\eta} = 0, \tag{B3}$$

so that

$$\mathscr{A}_1 = \frac{1}{4}\cos 2\eta\, \hat{L}\mathscr{A}_0. \tag{B4}$$

At order Υ^2 we have

$$\hat{L}\mathscr{A}_{0\tau} + \frac{i}{4}\cos^2 2\eta\, \hat{L}^2\mathscr{A}_0 + i\mathscr{A}_{2\eta\eta} = 0. \tag{B5}$$

In order to obtain a periodic-in-η solution of (B.5) for $\mathscr{A}_2$ one must take

$$\hat{L}\mathscr{A}_{0\tau} + \frac{i}{8}\hat{L}^2\mathscr{A}_0 = 0. \tag{B6}$$

The solvability condition in (B6) indicates that the rectified part of $\cos^2 2\eta$ is balanced by the slow evolution of the large-scale field, $\mathscr{A}_0$. By restoring the dimensions in (B6) we obtain the strong dispersion approximation as given in (6.1b).

REFERENCES

Abramowitz, M. and I. A. Stegun. 1972. Handbook of Mathematical Functions, Wiley Interscience Publications. 1046 pp.

Brillouin, L. 1946. Wave Propagation in Periodic Structures, Dover, 255 pp.

D'Asaro, E. A. 1989. The decay of wind forced mixed layer inertial oscillations due to the β-effect. J. Geophys. Res., *94,* 2045–2056.

—— 1995a. Upper-ocean inertial currents forced by a strong storm. Part II: Modeling. J. Phys. Oceanogr., *25,* 2937–2952.

—— 1995b. Upper-ocean inertial currents forced by a strong storm. Part III: Interaction of inertial currents and mesoscale eddies. J. Phys. Oceanogr., *25,* 2953–2958.

D'Asaro, E. A., C. C. Eriksen, M. D. Levine, P. P. Niiler, C. A. Paulson and P. van Meurs. 1995. Upper-ocean inertial currents forced by a strong storm. Part I: Data and comparisons with linear theory. J. Phys. Oceanogr., *25,* 2909–2936.

Gill, A. E. 1984. On the behavior of internal waves in the wakes of storms. J. Phys. Oceanogr., *14,* 1129–1151.

Klein, P. and A. M. Treguier. 1995. Dispersion of wind-induced inertial waves by a barotropic jet. J. Mar. Res., *53,* 1–22.

Kunze, E. 1985. Near inertial wave propagation in geostrophic shear. J. Phys. Oceanogr., *15,* 544–565.

Kunze, E., R. W. Schmitt and J. M. Toole. 1995. The energy balance in a warm-core ring's near-inertial critical layer. J. Phys. Oceanogr., *25,* 942–957.

Lee, D.-K. and P. P. Niiler. 1998. The inertial chimney: the near-inertial energy drainage from the ocean surface to the deep layer. Preprint.

McLachlan, N. W. 1947. Theory and Applications of Mathieu Functions, Oxford University Press, 401 pp.

Polzin, K. L. 1996. Statistics of the Richardson number: Mixing models and finestructure. J. Phys. Oceanogr., *26,* 1409–1425.

Rubenstein, D. H. and G. O. Roberts. 1986. Scattering of inertial waves by an ocean front. J. Phys. Oceanogr., *16,* 121–131.

Shirts, R. B. 1993. Algorithm 721—MTIEU1 and MTIEU2—two subroutines to compute eigenvalues and solutions to the Mathieu differential equation for noninteger and integer order. ACM Transactions on Mathematical Software, *19,* 389–404. See also http://gams.nist.gov.

van Meurs, P. 1998. Interactions between near-inertial mixing layer currents and the mesoscale: The importance of spatial variabilities in the corticity field. J. Phys. Oceanogr., (submitted).

Wang, D. P. 1991. Generation and propagation of inertial waves in the subtropical front. J. Mar. Res., *49,* 619–663.

Weller, R. A., D. L. Rudnick, C. C. Eriksen, K. L. Polzin, N. S. Oakey, J. W. Toole, R. W. Schmitt and R. T. Pollard. 1991. Forced ocean response during the Frontal Air-Sea Interaction Experiment. J. Geophys. Res., *96,* 8611–8638.

Young, W. R. and M. Ben Jelloul. 1997. Propagation of near-inertial oscillations through a geostrophic flow. J. Mar. Res., *55,* 735–766.

Zervakis, V. and M. Levine. 1995. Near-inertial energy propagation from the mixed layer: theoretical considerations. J. Phys. Oceanogr., *25,* 2872–2889.

Received: *13 May 1997;* revised: *9 September 1997.*